

Please cite the Published Version

Lin, Z, Pokrajac, D, Guo, Y, Liao, C and Tang, T (2020) Near-trapping effect of wave-cylinders interaction on pore water pressure and liquefaction around a cylinder array. *Ocean Engineering*, 218. ISSN 0029-8018

DOI: <https://doi.org/10.1016/j.oceaneng.2020.108047>

Publisher: Elsevier

Version: Accepted Version

Downloaded from: <https://e-space.mmu.ac.uk/628315/>

Usage rights:  [Creative Commons: Attribution-Noncommercial-No Derivative Works 4.0](https://creativecommons.org/licenses/by-nc-nd/4.0/)

Additional Information: This is an Author Accepted Manuscript of a paper accepted for publication in *Ocean Engineering*, published by and copyright Elsevier.

Enquiries:

If you have questions about this document, contact openresearch@mmu.ac.uk. Please include the URL of the record in e-space. If you believe that your, or a third party's rights have been compromised through this document please see our Take Down policy (available from <https://www.mmu.ac.uk/library/using-the-library/policies-and-guidelines>)

1 **Near-trapping effect of wave-cylinders interaction on pore water pressure and liquefaction**
2 **around a cylinder array**

3 Zaibin Lin^a, Dubravka Pokrajac^b, Yakun Guo^c, Chencong Liao^d, Tian Tang^e

- 4
- 5 a. Now Centre for Mathematical Modelling and Flow Analysis, School of Computing,
6 Mathematics and Digital Technology, Manchester Metropolitan University, Manchester, M1
7 5GD, United Kingdom
8 Formerly School of Engineering, University of Aberdeen, AB24 3UE, UK
9 Corresponding author: zaibin.lin@gmail.com,
- 10 b. School of Engineering, University of Aberdeen, AB24 3UE, UK
- 11 c. Faculty of Engineering and Informatics, University of Bradford, BD7 1DP, UK,
- 12 d. Collaborative Innovation Centre for Advanced Ship and Deep-Sea Exploration, State Key
13 Laboratory of Ocean Engineering, Department of Civil Engineering, Shanghai Jiao Tong
14 University, Shanghai, 200240, China
- 15 e. Bekaert Technology Centre, Bekaert Company, Zvevegem, Belgium
- 16
- 17

18 **Abstract:** The near-trapping effects on wave-induced dynamic seabed response and liquefaction
19 close to a multi-cylinder foundation in storm wave conditions are examined. Momentary liquefaction
20 near multi-cylinder structures is simulated using an integrated wave-structure-seabed interaction
21 model. The proposed model is firstly validated for the case of interaction of wave and a four-cylinder
22 structure, with a good agreement with available experimental measurements. The validated model is
23 then applied to investigate the seabed response around a four-cylinder structure at 0° and 45°
24 incident angles. The comparison of liquefaction potential around individual cylinders in an array
25 shows that downstream cylinder is well protected from liquefaction by upstream cylinders. For a
26 range of incident wave parameters, the comparison with the results for a single pile shows the
27 amplification of pressure within the seabed induced by progressive wave. This phenomenon is
28 similar to the near-trapping phenomenon of free surface elevation within a cylinder array.

29

30 **Key words:** Wave-Structure-Seabed Interaction (WSSI); seabed response; four-cylinder foundation;
31 near-trapping phenomenon; momentary liquefaction

32

33 **1. Introduction**

34 Multi-cylinder structures, one of the most common offshore foundations, are vulnerable to
35 environmental impact of waves and currents, and the associated dynamic seabed response. The
36 wave-induced run-up, forcing, and seabed instability around foundations may result in the collapse
37 of offshore structures. For the critical centre-to-centre spacing between cylinders and a given range
38 of incident wave numbers, the near-trapping phenomenon can occur within an array of cylinder (Ohl
39 et al., 2001a). This phenomenon causes the local amplification of wave amplitude, which occurs due
40 to the trapping of undisturbed incident wave inside an array of cylinders. As a result, the
41 wave-induced run-up and forcing, as well as the associated seabed response in the vicinity of
42 multi-cylinder foundation can be significantly greater than in the case of single cylinder (Kamath et

43 al., 2016). The effect of these phenomena on the safety of offshore structures and their foundations is
44 of particular interest and important due to the increasing applications of multi-cylinder foundations
45 in offshore engineering.

46
47 Near-trapping phenomenon is a dominant factor considered in the design of sufficient air gap under
48 the deck of offshore structures. This phenomenon has been systematically and intensively
49 investigated by numerous researchers. To obtain the velocity potential surrounding the various
50 arrangements of two cylinders and force components induced by linear water waves, Spring and
51 Monkmeyer (1974) analytically solved the potential theory formulations using a direct matrix
52 solution and multiple scattering (Twersky, 1952). Based on the same assumption used in Spring and
53 Monkmeyer (1974), Linton and Evans (1990) simplified the theory, and proposed new formulae to
54 estimate the free surface elevation around an array of cylinders, together with new formulae to
55 calculate the first and second-order mean forces. Using eigenfunction expansions and an integral
56 representation, Malenica et al. (1999) introduced a semi-analytical approach to solve for velocity
57 potential with an incident monochromatic wave for estimating the second-order wave diffraction in
58 the vicinity of an array of circular cylinders. The experimental investigations of the near-trapping
59 phenomenon under regular and irregular incident waves with two incident wave directions are
60 analysed by Ohl et al. (2001a; b) who pointed out that Malenica et al. (1999) overestimated the
61 second order amplitude under the regular wave with 45° heading.

62
63 The rapid development of computing resources and techniques of Computational Fluid Dynamics
64 (CFD) has made the full scale three-dimensional (3D) simulation of wave-structure interaction in
65 ocean/offshore engineering problems possible. Extensive investigations were carried out to study
66 these problems. An open source CFD model, REEF3D, was developed to investigate fully nonlinear
67 wave-structure interaction with various arrangements of cylinder groups, including two cylinders in
68 tandem (Kamath et al., 2015; Bihs et al., 2016) and four cylinders in an array (Kamath et al., 2016).
69 In REEF3D continuity equations and Reynolds-averaged Navier-Stokes (RANS) equations, together
70 with $k-\omega$ turbulence model are discretised using Finite Difference Method (FDM). The free surface
71 between water and air is tracked by Level Set Method (LSM). In the study of Kamath et al. (2016), a
72 pronounced amplification of the wave force on upstream cylinder was found by comparing the
73 simulated results for the cases with and without the downstream cylinders in a four-cylinder array.
74 Another broadly adopted open access CFD code in coastal/offshore engineering is the OpenFOAM
75 with free C++ library for solving a wide range of fluid flow and solid mechanics problems using
76 Finite Volume Method (FVM). With the help of the open source wave generation tool waves2Foam
77 (Jacobsen et al., 2012) in OpenFOAM and the application of a slip boundary condition on the
78 cylinder surface, Paulsen et al. (2014b) performed the intensive investigations of the fully nonlinear
79 wave-cylinder interaction for a range of Keulegan–Carpenter (KC) numbers ($KC = U_{z=0}T/D$, where
80 $U_{z=0}$ is the velocity amplitude at $z=0$ with z pointing vertically, T is wave period, and D is the
81 diameter of cylinder, Sumer and Fredsøe 2006). By analysing the numerical results, it was concluded
82 that the process of return flow from the back of cylinder and the passage of the wave crest made the
83 dominant contributions to the occurrence of secondary load cycle. For the purpose of more efficient
84 computation, Paulsen et al. (2014a) proposed an innovative and fully nonlinear domain

85 decomposition approach, which involves coupling potential flow theory model (OceanWave3D,
86 Engsig-Karup et al., 2009) and waves2Foam library. The good agreement between numerical and
87 experimental results for irregular waves has demonstrated the accuracy and applicability of the
88 coupled model. Chen et al. (2014) also elaborated a comprehensive study for exploring the
89 applicability and capacity of OpenFOAM in evaluating fully nonlinear wave-cylinder interaction
90 under regular and focused waves. Moreover, both wave generation and active absorbing boundaries
91 were developed in Higuera et al. (2013a) (IHFOAM) for simulating wave-induced coastal
92 engineering processes (Higuera et al., 2013b), and wave interaction with porous structures (Higuera
93 et al., 2014a; Higuera et al., 2014b). A new moving boundary decomposed into multi-paddles and an
94 enhanced active wave absorption boundary were integrated into IHFOAM (Higuera et al., 2015). All
95 aforementioned research has been mainly concerned with wave interaction with coastal/offshore
96 structures. However, the attention should also be paid to another important issue, namely the wave
97 induced dynamic response in a porous seabed which occurs as a result of fully nonlinear
98 wave-structure interactions.

99

100 Seabed stability in the vicinity of coastal/offshore structures is one of the most important issues in
101 engineering design (Sumer and Fredsøe, 2002; Jeng, 2013; Sumer, 2014; Jeng, 2018). At the early
102 stage of seabed stability research, analytical approximations on the basis of poro-elastic Biot's theory
103 (Biot, 1941) were extensively used for investigating wave-induced seabed response. A considerable
104 amount of both the theoretical and experimental porous seabed research before 2003 has been
105 reviewed and summarized in Jeng (2003). In recent years, the applicability of three different soil
106 models, including fully dynamic (FD), partially dynamic (PD), and quasi-static (QS) model, was
107 investigated in Ulker and Rahman (2009) and Ulker et al. (2009). Their conclusions are consistent
108 with Jeng and Cha (2003), who showed that the maximum discrepancy between the calculated
109 results is within 3%. and they proposed the applicability for the three above-mentioned models in
110 partially/fully saturated porous seabed. Considering the combined effect of current and nonlinear
111 wave, Liao et al. (2013) proposed an analytical approximation to investigate the soil response within
112 a porous seabed, and concluded that this effect had a considerable impact in the upper zone beneath
113 seabed surface. However, due to underlying assumptions and simplifications these analytical
114 approximations are not able to fully describe the complicated process of wave-induced seabed
115 stability in the proximity of coastal/offshore structures.

116

117 Due to its practical importance and engineering applications, extensive laboratory experimental
118 modelling studies have been conducted to investigate wave-induced soil response in a porous seabed.
119 To understand the mechanism of pore water pressure and scour around a mono-pile foundation, Qi
120 and Gao (2014) performed experimental studies with various combined wave and current parameters.
121 Liu et al. (2015) conducted laboratory experiment in a one-dimensional (1-D) soil column to
122 examine the pore pressure development under sinusoidal wave pressure applied at one end of the
123 column. The thickness of sandy deposit was slightly reduced after a long-term dynamic wave loading.
124 The oscillatory excess pore pressure within a well-mixed seabed, consisting of silt and sand, and the
125 influence of the ratio of sand/silt in mixture were experimentally studied by Zhang et al. (2016) with
126 a series of incident waves. Recently, Sun et al. (2019) conducted laboratory experiments to

127 investigate the dynamic soil response and liquefaction potential around a buried pipeline in a trench
128 layer. In the context of wave-induced soil response, the experimental studies have the capacity of
129 directly capturing the realistic behaviour. However, the scope of physical experiments is limited by
130 scale-effects and cost.

131

132 Numerical modelling is the effective alternative approach adopted by numerous researchers. Without
133 considering the wave diffraction and reflection, Li et al. (2011) estimated the wave-induced pore
134 pressure around pile foundation by solving 3D Biot's equation using FEM. Hereafter, a series of
135 investigations by Jeng and his co-workers has been performed to examine dynamic behaviour of the
136 soil in a marine seabed around coastal/offshore structures, such as pipeline (Zhao et al., 2016; Lin et
137 al., 2016), breakwaters (Zhang et al., 2011; Jeng et al., 2013; Ye et al., 2013; Ye et al., 2016), and pile
138 supported structures (Sui et al., 2017, 2019; Zhao et al., 2017). In all these studies, the equations
139 governing the motion of two-phase fluid (RANS and VOF) and the response of seabed were solved
140 by FVM and FEM, respectively. Another monolithically integrated model solving both types of
141 governing equations by using FEM approach was proposed in Lin et al. (2016) to investigate the
142 wave-induced seabed instability (liquefaction potential) in the neighbourhood of partially/fully
143 buried pipeline. Liu et al. (2007) were first to develop a soil solver in OpenFOAM based on the
144 discretised Biot's equation, using FVM for the estimation of wave-induced seabed response
145 surrounding submerged structure. However, this coupled model could not run in a parallel manner as
146 demonstrated in Liu et al. (2007). An extension of poro-elastic model to poro-elasto-plasticity soil
147 model was proposed and implemented in OpenFOAM in Tang (2014), Tang and Heddal (2014), and
148 Tang et al. (2015). In Li et al. (2018) this proposed model was used to investigate the wave-induced
149 momentary liquefaction in the vicinity of gravity-based structure considering the linear elastic
150 structure response of the foundation. For the research on wave-induced seabed response around
151 single/multi-cylinder foundations, Chang and Jeng (2014) performed a numerical investigation of the
152 seabed instability close to a high-rising structure foundation, and concluded that the replacement of
153 surrounding soil layer with a coarse sand layer with greater permeability was a sufficient protection
154 from potential liquefaction. Most recently, by integrating FUNWAVE (Wei et al., 1999; Shi et al.,
155 2001; Kirby et al., 2003) and fully dynamic (FD) form of Biot's equations, Sui et al. (2016)
156 discussed the dynamic soil response caused by small steepness wave. It was concluded that the
157 dynamic behaviour of a porous seabed and a mono-pile were all governed by fully dynamic form of
158 Biot's equations. Lin et al. (2017) proposed a one-way integrated model solving both wave and soil
159 model in OpenFOAM to investigate the nonlinear wave-induced soil response around a
160 large-diameter mono-pile foundation. It was concluded that increasing penetration depth of
161 mono-pile foundation resulted in the decrease of the maximum liquefaction depth around foundation.
162 Recently, the investigation in Zhang et al. (2017) concluded that the existence of upstream piles in an
163 offshore platform may reduce the wave velocity when it approaches downstream piles. Moreover,
164 Tong et al. (2017) suggested that the existence of upstream pile may reduce the wave-induced seabed
165 response near the downstream pile in a twin pile group. Though many studies have been conducted
166 to examine the wave-induced soil response of a porous seabed around various coastal/offshore
167 structures, the soil dynamics in a porous seabed in a multi-cylinder foundation subject to storm wave
168 has not yet been fully understood. A very recent work on the coupled Fluid-Structure-Seabed model

169 has been proposed by Duan et al. (2019), who used IHFOAM and u - p approximation for the
 170 investigation of the seabed response near mono-pile foundation in combined wave-current
 171 environment.

172

173 This study focuses on the near-trapping effects on dynamic seabed response and liquefaction close to
 174 a multi-cylinder foundation in storm wave condition, which has not been studied yet. The segregated
 175 FVM solver proposed in Lin et al. (2017), which incorporates waves2Foam and Biot's equations, is
 176 adopted here and further applied to investigate the unknown issue of storm wave-induced soil
 177 response around a multi-cylinder foundation. The governing equations for wave and seabed model
 178 are described in the Section 2. In Section 3, the simulation of near-trapping phenomenon is validated
 179 in detail against available experimental results. Section 4 discusses the distribution of wave pressure,
 180 free surface elevation, and liquefaction depth in the vicinity of multi-cylinder structure under two
 181 incident wave headings and compares these results with those obtained for a single cylinder. The
 182 main conclusions are summarized in Section 5.

183

184 2. Numerical model

185 Two numerical domains are used in the present study, one for incident wave at 0° , as shown in Figure
 186 1, and another one for 45° , as shown in Figure 2. Each numerical domain has two sub-domains,
 187 namely a two-phase fluid flow domain (including water and air) and a porous seabed domain. The
 188 two-phase fluid flow domain above the seabed is simulated using waves2Foam (Jacobsen et al.,
 189 2012), while the porous seabed behaviour is governed by Quasi-Static (QS) Biot's model. The two
 190 sub-models are integrated through the extended General Grid Interpolation (GGI), which
 191 incorporates the interpolation of the face and point from zone to zone in terms of non-matched mesh
 192 at the interface of flow and seabed sub-domain (Tuković et al., 2014).

193

194 2.1 Wave model

195 The two-phase flow above the seabed surface is simulated by the following mass and momentum
 196 equations together with a free-surface tracing function, namely Volume of Fluid (Hirt and Nichols,
 197 1981; Berberović et al., 2009)

$$\nabla \cdot \mathbf{u} = 0 \quad (1)$$

$$\frac{\partial \rho \mathbf{u}}{\partial t} + \nabla \cdot (\rho \mathbf{u}) \mathbf{u}^T = -\nabla p^* - (\mathbf{g} \cdot \mathbf{x}) \nabla \rho + \nabla \cdot (\mu \nabla \mathbf{u}) \quad (2)$$

$$\frac{\partial \alpha}{\partial t} + \nabla \cdot \mathbf{u} \alpha + \nabla \cdot \mathbf{u}_r \alpha (1 - \alpha) = 0 \quad (3)$$

198 where \mathbf{u} is the flow velocity; ρ is the density of fluid; t is the time; $p^* = p - \rho \mathbf{g} \cdot \mathbf{x}$ is the wave
 199 pressure in excess of static pressure; \mathbf{g} is the gravitational acceleration; \mathbf{x} is the Cartesian
 200 coordinate vector; p is the pressure; μ is dynamic viscosity; $\mathbf{u}_r = \mathbf{u}_w - \mathbf{u}_a$ is the relative flow
 201 velocity vector (\mathbf{u}_w and \mathbf{u}_a are velocity of water and air phase, respectively, Berberović et al.,
 202 2009); α is the volume fraction function. $\alpha = 1$ indicates the computational cell is occupied by
 203 water, while $\alpha = 0$ denotes that a cell is full of air, and the cell with water-air mixture has $0 < \alpha <$
 204 1. The momentary fluid density and dynamic viscosity are obtained from following equations:

$$\rho = \alpha \rho_w + \rho_a (1 - \alpha) \quad (4)$$

$$\mu = \alpha\mu_w + \mu_a(1 - \alpha) \quad (5)$$

205 where the sub-indices w and a correspond to water and air, respectively.

206

207 At the seabed, mono-pile surface, and lateral boundaries of numerical wave flume, the boundary
 208 layer effects are not considered and hence slip boundary is adopted as boundary condition. This is
 209 consistent with the study performed by Paulsen et al. (2014b). A pressure outlet condition is specified
 210 at the atmospheric boundary on the top of the two-phase flow domain, where air and water can flow
 211 out and zero-gradient is applied on the velocity vector fields, but only air can flow in, with a
 212 fixed-value condition and water volume fraction being 0 (Chen et al., 2014). For the detailed
 213 description of wave generation (inlet boundary) and wave absorption (outlet boundary) zone, the
 214 reader is referred to Jacobsen et al. (2012).

215

216 2.2 Seabed model

217 In the hydraulically isotropic porous seabed, the wave-induced dynamic behaviour of soil is
 218 governed by QS Biot's equations (Biot, 1941). The mass balance equation adopted in present study is

$$\nabla^2 p_p - \frac{\gamma_w n_s \beta_s}{k_s} \frac{\partial p_p}{\partial t} = \frac{\gamma_w}{k_s} \frac{\partial \varepsilon_s}{\partial t} \quad (6)$$

219 where p_p is the pore water pressure, γ_w is the unit weight of water, n_s is the porosity of soil, and
 220 k_s is the Darcy's permeability. The compressibility of pore fluid β_s and the volumetric strain ε_s
 221 are defined, respectively, as:

$$\beta_s = \frac{1}{K_w} + \frac{1 - S_r}{P_{w0}} \quad (7)$$

$$\varepsilon_s = \nabla \cdot \mathbf{v} = \frac{\partial u_s}{\partial x} + \frac{\partial v_s}{\partial y} + \frac{\partial w_s}{\partial z} \quad (8)$$

222 where K_w is the true bulk modulus of elasticity of water (taken as 2×10^9 N/m², Yamamoto et al.,
 223 1978); S_r is the saturation degree of soil; P_{w0} is the absolute pore water pressure; $\mathbf{v} = (u_s, v_s, w_s)$
 224 is the vector of soil displacement.

225

226 The force equilibrium equation for a poro-elastic seabed can be expressed as:

$$G \nabla^2 \mathbf{v} + \frac{G}{1 - 2\nu} \nabla \varepsilon_s = \nabla p_p \quad (9)$$

227 where G is the shear modulus of soil in relation to Young's modulus (E) and Poisson's ratio (ν):

$$G = \frac{E}{2(1 + \nu)} \quad (10)$$

228

229 The stress-strain relationships for a poro-elastic seabed can be determined on the basis of Hooke's
 230 law as

$$\sigma'_x = 2G \left(\frac{\partial u_s}{\partial x} + \frac{\nu}{1 - 2\nu} \varepsilon_s \right), \quad \sigma'_y = 2G \left(\frac{\partial v_s}{\partial y} + \frac{\nu}{1 - 2\nu} \varepsilon_s \right) \quad (11)$$

$$\sigma'_z = 2G \left(\frac{\partial w_s}{\partial z} + \frac{\nu}{1 - 2\nu} \varepsilon_s \right), \quad \tau_{xy} = \tau_{yx} = G \left(\frac{\partial u_s}{\partial y} + \frac{\partial v_s}{\partial x} \right) \quad (12)$$

$$\tau_{xz} = \tau_{zx} = G \left(\frac{\partial u_s}{\partial z} + \frac{\partial w_s}{\partial x} \right), \tau_{yz} = \tau_{zy} = G \left(\frac{\partial v_s}{\partial z} + \frac{\partial w_s}{\partial y} \right) \quad (13)$$

231 where σ'_i is effective normal stress, τ_{ij} is shear stress, the subscripts $i,j=x,y,z$ denote the directions
 232 of Cartesian coordinates.

233

234 To solve QS Biot's equations, the following boundary conditions are prescribed at the boundaries of
 235 porous seabed domain and cylinder surface. The upper boundary of seabed domain, namely seabed
 236 surface ($y=0$ in Figure 2 and Figure 3), is the pressure boundary with the pore water pressure, p_p ,
 237 equal wave pressure, p^* . Furthermore, the vertical shear stresses and effective normal stress are set
 238 as 0 at the seabed surface:

$$\sigma'_y = \tau_{xy} = \tau_{yz} = 0, p_p = p^* \text{ at } y = 0 \quad (14)$$

239

240 The bottom of seabed ($y = -h_s$, where h_s is the soil depth, Figure 2 and Figure 3) is selected as an
 241 impermeable rigid boundary, where no vertical flow and no soil displacement occur:

$$u_s = v_s = w_s = \frac{\partial p_p}{\partial y} = 0 \text{ at } y = -h_s \quad (15)$$

242

243 The lateral boundaries of seabed domain are set as impermeable rigid boundaries (Chang and Jeng,
 244 2014):

$$u_s = v_s = w_s = 0, \frac{\partial p_p}{\partial x} = 0 \text{ at } x = 0 \text{ and } x = L_s \quad (16)$$

$$u_s = v_s = w_s = 0, \frac{\partial p_p}{\partial z} = 0 \text{ at } z = -W_s/2 \text{ and } z = W_s/2 \quad (17)$$

245

246 The sizes of both flow and seabed domain are designed with sufficient length (L_s) and width (W_s) to
 247 eliminate the effect from lateral boundaries. Ye and Jeng (2012) suggested that the length of seabed
 248 domain should be more than double wavelength to avoid the effect of lateral boundaries on the
 249 simulation results within zone of interest, so L_s and W_s are taken as 4.5 times the wavelength (L_w)
 250 and 16 times the diameter of cylinder (D). The centres of two different layouts of four cylinders in
 251 Figure 2 and Figure 3 and the centres of both flow and seabed domains coincide, so the simulation
 252 results around cylinders are not affected by the lateral boundary conditions. In addition, the cylinders
 253 are assumed to be rigid impermeable objects and their surfaces are treated as no-flow boundary
 254 conditions with zero pore water pressure gradient:

$$\frac{\partial p_p}{\partial \mathbf{n}} = 0 \quad (18)$$

255 where \mathbf{n} is the direction normal to the surface of a cylinder. No-flow boundary condition is
 256 generally adopted for the surface of rigid object buried/penetrated into a porous seabed (Chang and
 257 Jeng, 2014; Lin et al., 2016). Therefore, the interaction between soil and cylinder foundation, which
 258 is caused by the fluid-induced cylinder vibration, is not considered here. For the related works
 259 considering two-way coupled soil-structure interactions, readers are referred to Tong et al. (2019).

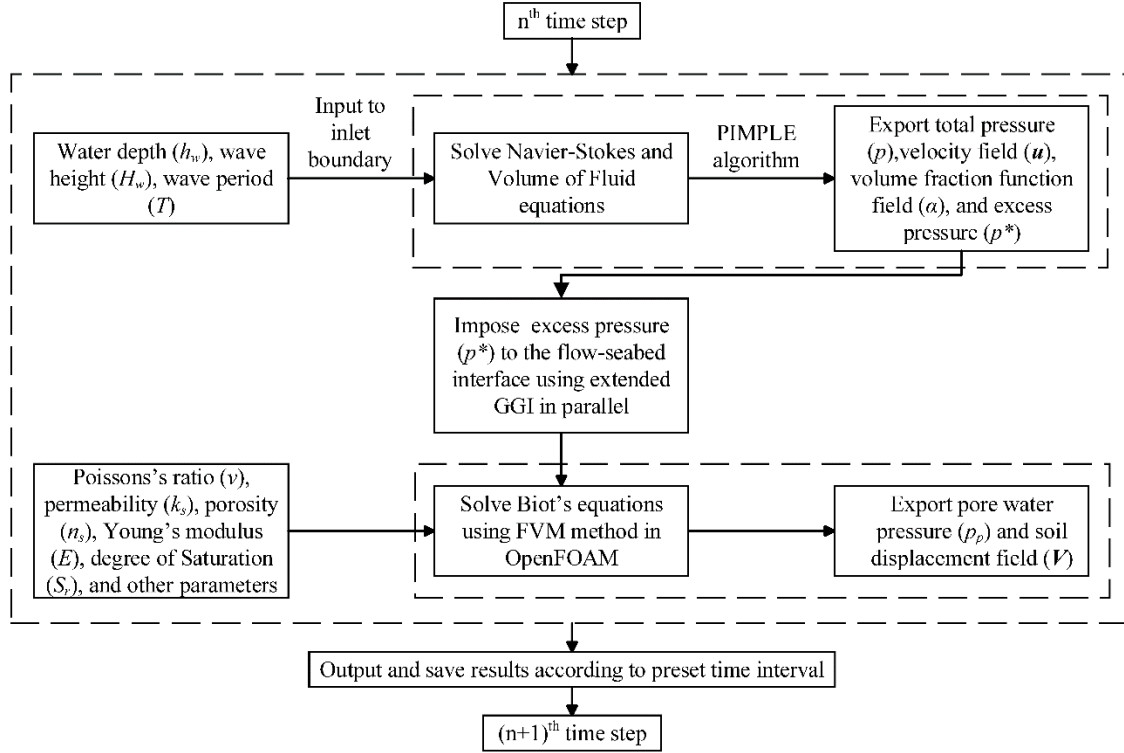


Figure 1 Integrated process of WSSI model

260

261 2.3 Integrated process between wave and seabed model

262 The aforementioned sub-models are integrated through one-way process, as shown in Figure 1.
 263 Within one time step the integrated model solves the wave and seabed models individually: the
 264 dynamic wave pressure (p^*) at the flow-seabed interface calculated by the wave model
 265 (waves2Foam) is imposed as the boundary condition to the seabed model by using extended general
 266 grid interpolation (GGI) in parallel (Tuković et al., 2014). The detailed interpretation of integration
 267 process can be found in Lin et al. (2017). In the present study, the adjustable time step for both flow
 268 and seabed model is determined by Courant-Friedrichs-Lewy (CFL) condition with the value of 0.5.

269

270

Table 1 Wave and cylinder parameters for validation

Experiments	Case	Wave amplitude, A (m)	Wave period, T (s)	Water depth, h_w (m)	Cylinder diameter, D (m)	$k_w r$	$k_w A$
Ohl et al. (2001b)	1	0.0925	1.25	2	0.406	0.524	0.238
	2	0.049					0.126
	3	0.0589	1.326	2	0.406	0.465	0.135

Note: k_w is wave number; r is cylinder radius.

271

272 **3. Validation**

273 The wave and soil components of the present integrated model have been validated for a mono-pile
 274 in Lin et al. (2017). In this section, the cases with an array of four cylinders are validated against the
 275 available experimental data for the two layouts shown in Figure 2 and Figure 3 with 0° and 45°

276 incident waves, respectively. The parameters for validation are listed in Table 1, where A is wave
 277 amplitude, T is wave period, D is cylinder diameter, k_w is wave number, and r is cylinder radius. For
 278 the validation of the soil model, readers are referred to Lin et al. (2017). Hence in this section, only
 279 the capability of the wave model to simulate the free surface elevation due to wave interaction with
 280 four cylinders is investigated.
 281

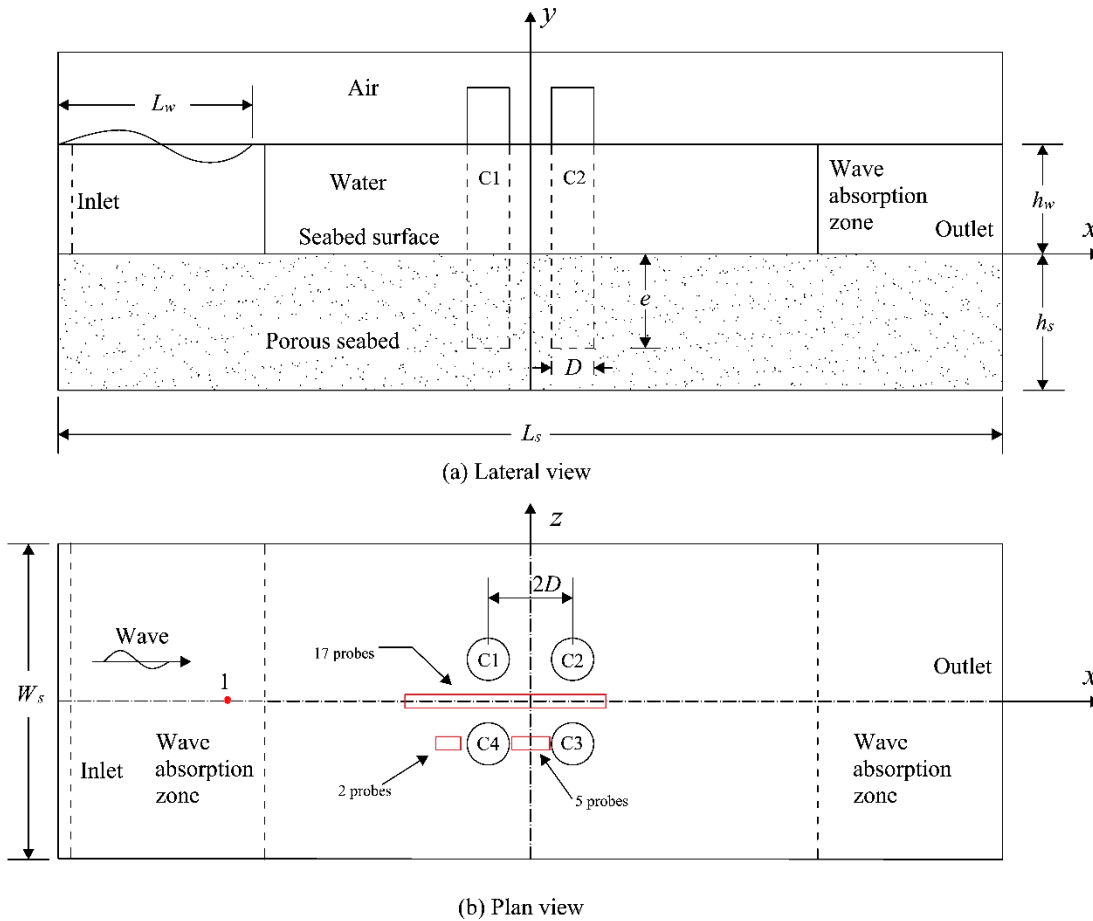


Figure 2 Sketch of the numerical wave tank with 0° incident wave. (a) Lateral view, (b) Plan view; the red dot 1 in plan view is the wave probe for measuring incident wave; the red rectangular zones are locations of other wave probes.

282

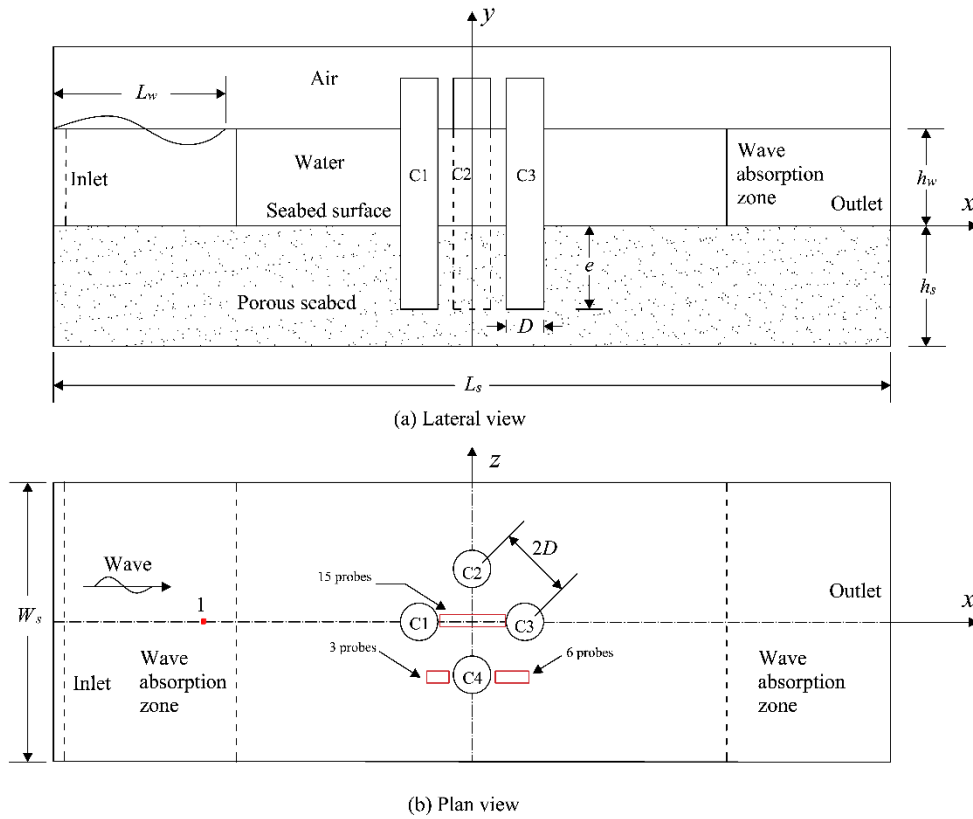


Figure 3 Sketch of the numerical wave tank with 45° incident wave. (a) Lateral view, (b) Plan view; the red dot 1 in plan view is the wave probe for measuring the incident wave; the red rectangular zones are locations of other wave probes.

283

284 The wave with two incident angles (0° and 45°) is considered. The experimental results performed in
 285 Ohl et al. (2001a) are used to validate free surface elevation surrounding an array of closely placed
 286 cylinders, where the space between the centres of two neighbouring cylinders is $2D$. The overall
 287 configurations of 3-D numerical domains are the same as those in Figure 2 and Figure 3, except that
 288 the soil subdomain is excluded, because it was not present in the experiments. The locations of wave
 289 probes are listed in Table 2. Near-trapping phenomenon is investigated for several different types of
 290 regular waves, including high and low steepness wave (see Table 1). The still water level and the
 291 diameter of the individual cylinders are 2m and 0.406m, respectively. In accordance with the studies
 292 of mesh sensitivity conducted in Paulsen et al. (2014b), the mesh for flow domain is refined to at
 293 least a resolution of 15 points per wave height for validations and further applications.

294

295 The first validation of wave model is carried out with Case 3 ($A = 0.0589$ m, $T = 1.325$ s) and the
 296 comparisons between simulated and experimental results are presented in Figure 4 for two incident
 297 regular waves (0° and 45°). It can be seen in Figure 4(a) that the free surface elevation (η) of the
 298 incident wave is in a fairly good agreement with the experimental result in an empty wave tank
 299 without any cylinders. For experiments/simulations with an array of cylinders the comparison in
 300 Figure 4(b) shows the simulated free surface elevation with 0° heading wave at wave probe A9
 301 agrees well with the experimental data, except for the slight discrepancy of the amount of water

302 merging after each wave crest and before the wave trough. It can be seen in Figure 5 that the small
 303 jump between wave crest and trough is caused by the small amount of water propagating from
 304 downstream to upstream. This small amount of water continues to propagate from the centre of the
 305 array to wave gauge A9, and merges with incoming wave trough, leading to the smaller free surface
 306 elevation at wave gauge A9. In Figure 4(c), the same experimental data at wave probe A9 are
 307 compared with the simulated results at the centre of array ($x=0, z=0$), which is only 0.05m away from
 308 A9, measured along the central line in the upstream direction. Figure 4(c) demonstrates that a slight
 309 shifting of the observation point yields a better agreement at the aforementioned discrepancy.

310
 311

Table 2 Wave probe locations in Figure 2 and Figure 3

Probe (0°)	x (m)	z (m)	Probe (45°)	x (m)	z (m)
1	-4.5	0	1	-4.5	0
B10	-1.15	0	D9	-0.35	0
B9	-1.05	0	E6	-0.3	0
B8	-0.95	0	D8	-0.25	0
B7	-0.85	0	E5	-0.2	0
B6	-0.75	0	D7	-0.15	0
B5	-0.65	0	E4	-0.1	0
B4	-0.55	0	D6	-0.05	0
B3	-0.45	0	D5	0	0
A12	-0.35	0	D4	0.05	0
A11	-0.25	0	E3	0.1	0
A10	-0.15	0	D3	0.15	0
A9	-0.05	0	E2	0.2	0
A8	0.05	0	D2	0.25	0
A7	0.15	0	E1	0.3	0
A6	0.25	0	D1	0.35	0
A5	0.35	0	D12	-0.325	-0.575
A4	0.45	0	D11	-0.275	-0.575
B12	-0.765	-0.407	D10	-0.225	-0.575
B11	-0.665	-0.407	E12	0.22	-0.575
B2	-0.15	-0.407	E11	0.32	-0.575
B1	-0.05	-0.407	E10	0.37	-0.575
A3	0.05	-0.407	E9	0.42	-0.575
A2	0.1	-0.407	E8	0.47	-0.575
A1	0.15	-0.407	E7	0.52	-0.575

312
 313

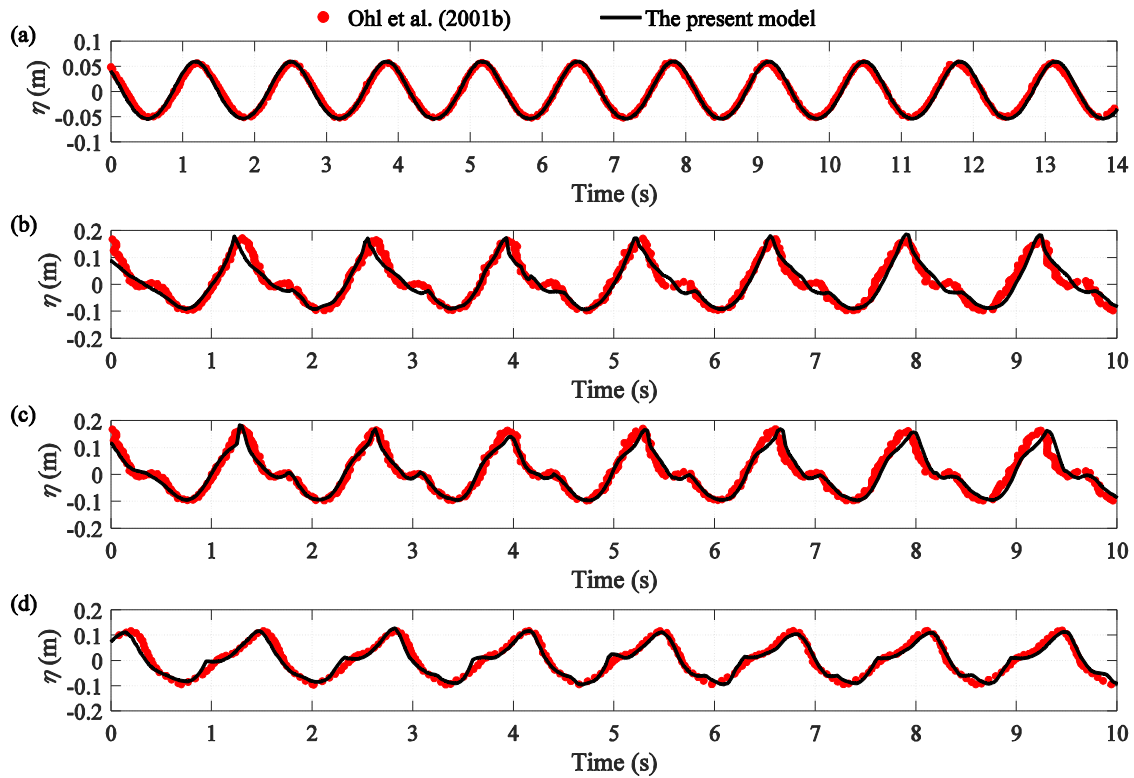
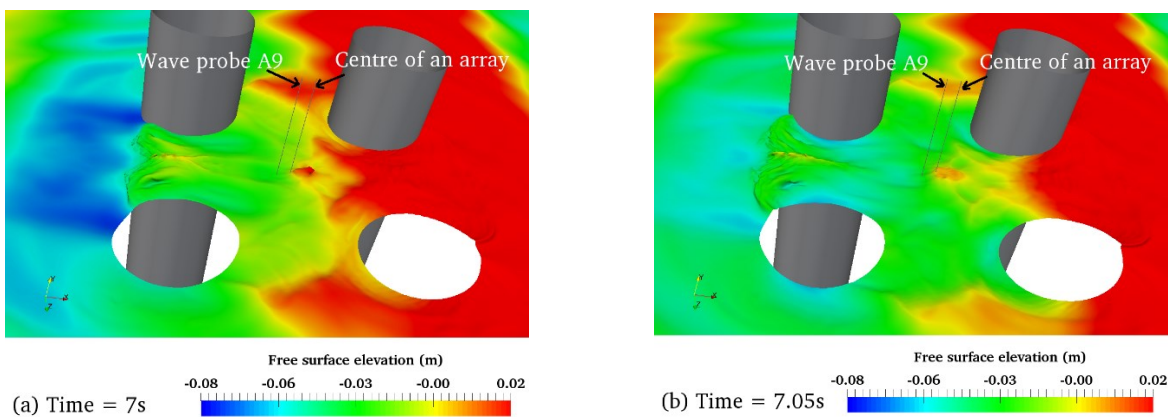


Figure 4 Time history of free surface elevation (η) of simulated and experimental results (Case 3 in Table 1). (a) Wave probe 1; (b) Wave probe A9 with 0° heading; (c) Centre of an array ($x=0$ and $z=0$) with 0° heading; (d) Wave probe E2, with 45° heading.

314

315 For a 45° heading wave with same parameters as 0° heading, the simulated and experimental results
 316 are compared in Figure 4(d), where a generally good agreement is demonstrated, with just a minor
 317 discrepancy before the arrival of individual wave crest. Comparison of the magnitude of both
 318 simulated and experimental results in Figure 4(b-d) with those for incident wave in Figure 4(a)
 319 shows that significant amplifications of the magnitude of both wave crest and wave trough resulted
 320 from wave-cylinders interaction. This amplification process of free surface elevation is termed
 321 near-trapping phenomenon. On the basis of above validations, it can be concluded that the
 322 developments of free surface elevation at typical locations within an array of cylinders are well
 323 predicted by numerical simulations.



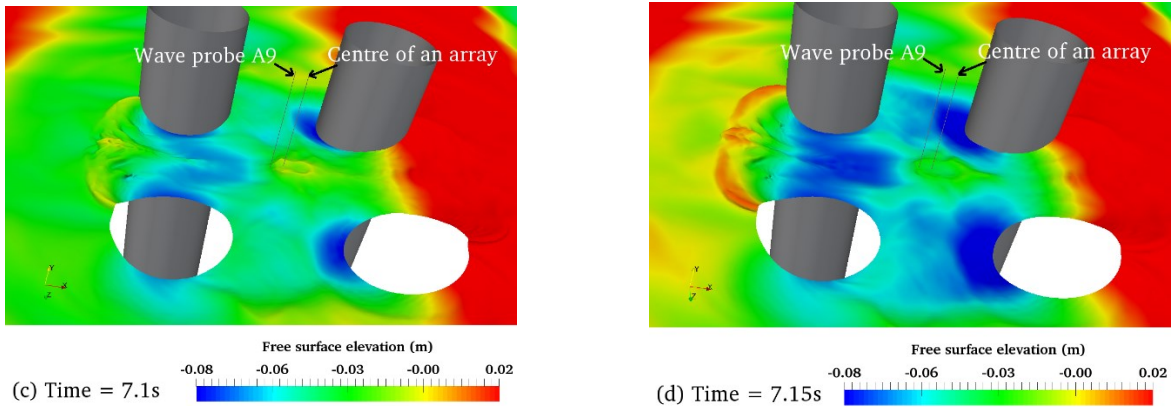


Figure 5 Snapshots of free surface elevation (η) at different moments for Case 3 in Table 1. (a) Time = 7s; (b) Time = 7.05s; (c) Time = 7.1s; (d) Time = 7.15s.

324

325 Further validations of wave model results for free surface elevation in the vicinity of cylinders are
 326 performed in frequency domain. For this purpose the time history of simulated results at various
 327 locations of wave probes indicated in Figure 2 and Figure 3 are processed by Fast Fourier
 328 Transforms (FFTs). The same processing procedure and approach used in Ohl et al. (2001a) are
 329 adopted here to extract the spectral peaks at single ($f = f_i$, f_i is incident wave frequency), double ($f =$
 330 $2f_i$), triple ($f = 3f_i$) incident wave frequencies, and all spectral components within the range of
 331 ($f \pm 0.25f_i$). These separated frequency components are termed first-, second-, and third-order
 332 harmonics, respectively. After that, each separated spectral component is further processed by
 333 Inverse FFTs (IFFTs) to obtain the corresponding time series, from which mean values of all the
 334 peaks are computed and compared with those for data measured at various locations of wave probes.

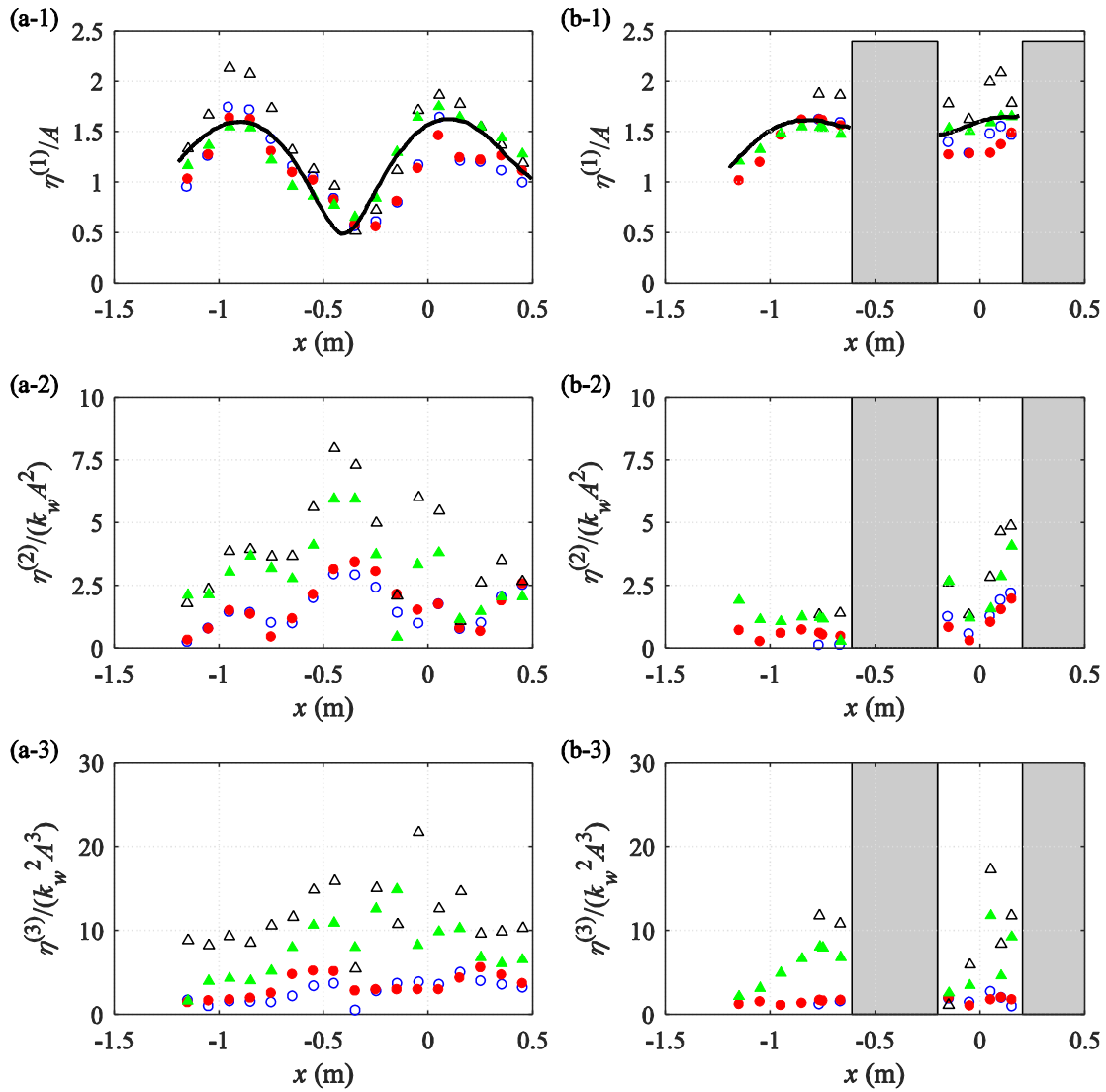


Figure 6 Comparison between simulated and experimental results of Case 1 and Case 2 with 0° heading. (1) First-order harmonics; (2) Second-order harmonics; (3) Third-order harmonics. (a) and (b) indicate the probes at central and lateral sides, respectively. \circ : case 1 in Ohl et al. (2001b); Δ : case 2 in Ohl et al. (2001b); \bullet : case 1 of present model; \blacktriangle : case 2 of present model; — : analytical solutions of Linton and Evans (1990).

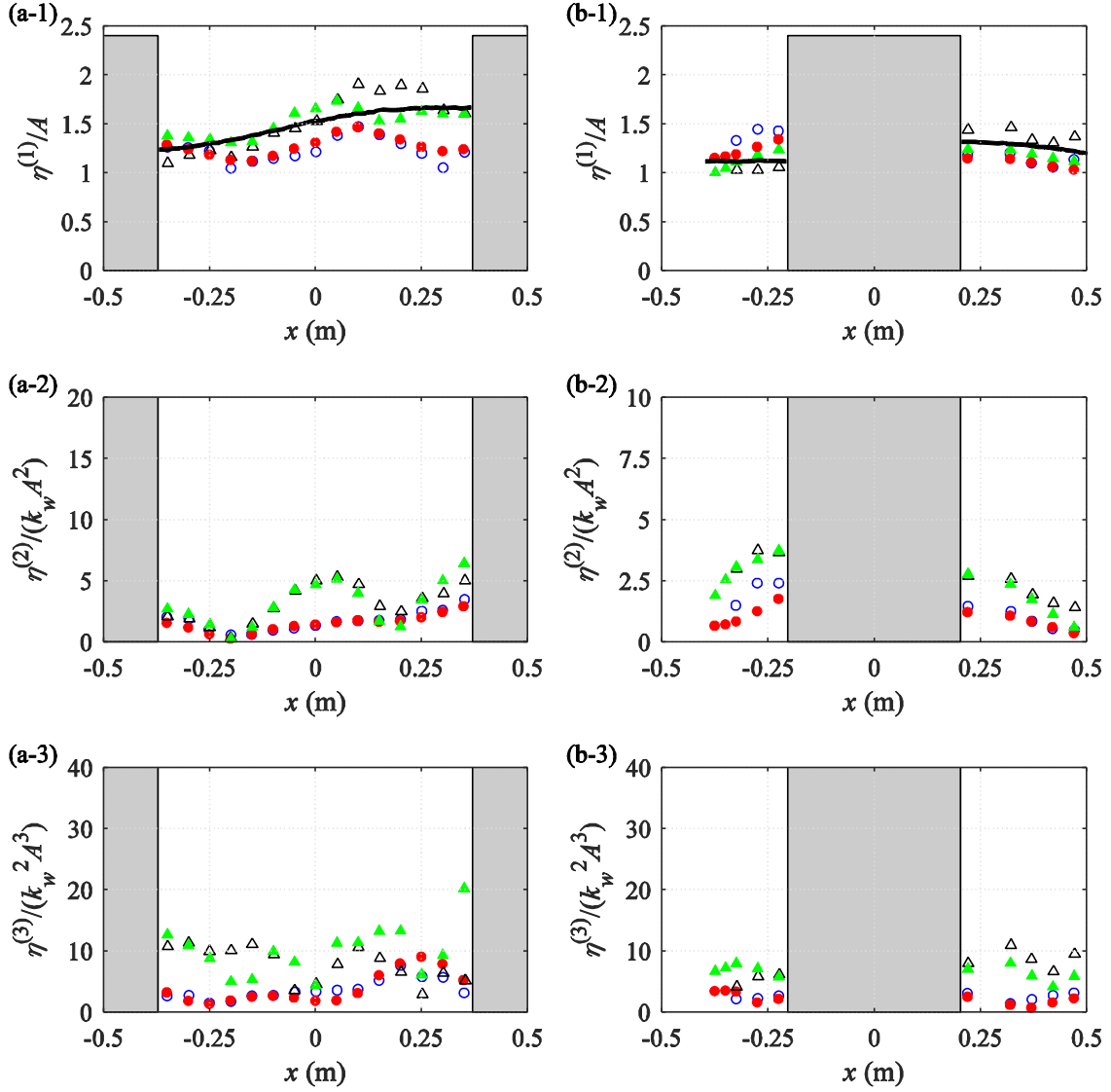


Figure 7 Comparison between simulated and experimental results for Case 1 and Case 2 with 45° heading. (1) First-order harmonics; (2) Second-order harmonics; (3) Third-order harmonics. Columns (a) and (b) indicate the probes at central and lateral sides, respectively. \circ : case 1 in Ohl et al. (2001b); Δ : case 2 in Ohl et al. (2001b); \bullet : case 1 of present model; \blacktriangle : case 2 of present model; — : analytical solutions of Linton and Evans (1990).

336

337 On the basis of aforementioned post-processing, additional comparisons of different order harmonics
 338 at various locations, up to third-order, are presented in Figure 6 for 0° incident angle and in Figure 7
 339 for 45° angle. The wave parameters of each validation case can be found in Table 1. For 0° heading
 340 (Figure 6) there are some discrepancies for Case 2 with smaller steepness wave, whereas the
 341 agreement for the Case 1 with greater steepness wave is much better. For the incident wave with 45°
 342 heading (Figure 7) there is good agreement for both Case 1 and Case 2. In both Figure 6 and Figure 7,
 343 the Case 1 with greater steepness wave has a better agreement with experimental results, rather than
 344 Case 2 with small wave steepness. From the comparisons of first-order component in Figure 6 and
 345 Figure 7, the evident amplification of free surface elevation, also named near-trapping phenomenon,

346 can be noticed along the central line and at lateral sides of four cylinders. Overall, it can be
 347 concluded that the near-trapping phenomenon has been well captured in the present numerical model
 348 that can be used to investigate dynamic seabed response around an array of cylinders.

349

350 4. Applications

351 Cylinder foundations supporting offshore wind turbines or platforms are usually protected from the
 352 onset of scour. When exposed to harsh ocean environments, scour protections surrounding cylinder
 353 foundations are vulnerable to liquefaction. However, the studies concerning liquefaction potential in
 354 the vicinity of closely placed cylinder foundations have not been reported yet. The previous
 355 investigation in Lin et al. (2017), performed for the wave condition from the Danish ‘Wave loads’
 356 project (Paulsen et al., 2014b), with $KC = 8.85$, and $k_w D = 0.2$, revealed that the maximum
 357 wave-induced liquefaction depth in the vicinity of a mono-pile foundation may occur at the lateral
 358 sides of the cylinder. In order to study liquefaction in the vicinity of an array of circular cylinders in
 359 storm wave conditions and compare it with the results for the single cylinder case, the same wave
 360 condition as in Lin et al. (2017) is adopted in the present study. The remaining parameters of incident
 361 wave used in present application are given in Table 3, with $k_w A$ being 0.14 in all simulations, and
 362 $k_w D$ ranging from 0.2 to 0.43. A constant $k_w A$ value and varying $k_w D$ values were adopted because of
 363 the results of Cong et al. (2015), who showed that near-trapping phenomenon is insensitive to $k_w A$,
 364 but highly sensitive to $k_w D$. The soil parameters used in this study are listed in Table 4. For the
 365 studies of varying soil parameters, readers are referred to Chang and Jeng (2014) for details.
 366 Individual cylinders are assumed to be rigid objects, and the movement of the cylinder foundations is
 367 not simulated. Two layouts of four cylinders investigated in this section are shown in Figure 2 and
 368 Figure 3. The location of a point along the perimeter of a cylinder is defined by its angle θ , as shown
 369 in Figure 8.

370

371

Table 3 Wave properties for the investigation of wave-cylinders-seabed interaction

Case	Wave amplitude, A (m)	Wave period, T (s)	Wave length, L_w (m)	$k_w D$	Water depth, h_w (m)
1	2.43	9.2	108.45	0.35	
2	2.88	10.5	129.12	0.29	
3	3.425	12.05	153.12	0.25	20
4	4.215	13.6	188.5	0.2	
5	1.94	7.88	86.79	0.43	

372

373

Table 4 Parameters for seabed and cylinders

Seabed characteristics			
Seabed thickness, h_s (m)	38	Poisson’s ratio, ν	0.4
Young’s modulus, E (Pa)	2.8×10^8	Permeability, k (m/s)	1×10^{-4}
Degree of saturation, S_r	0.98	Soil porosity, n_s	0.38
Cylinder characteristics			
Diameter, D (m)	6	Penetration depth, e (m)	18

374
375

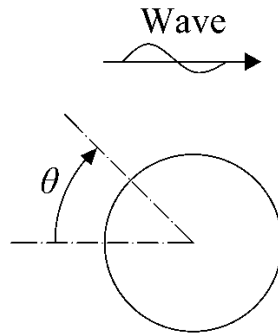


Figure 8 θ -location around a cylinder

376

377 4.1 Liquefaction development around cylinders in an array

378 Momentary liquefaction can take place at a point at a depth $L_d (= -y)$ beneath the seabed surface
 379 when the difference between the pore pressure at this level, p_p , and the pressure on a seabed surface
 380 above the point, P_b , becomes sufficiently large to balance or even exceed the overburden soil weight
 381 per unit area. As a result soil matrix becomes incapable of carrying any load and momentary
 382 liquefaction occurs. This process contributes to the scour around a cylinder founded in a sand bed
 383 (Tonkin et al., 2003). It should be noted that both the p_p , and P_b denote pressure in excess of
 384 hydrostatic pressure, so that the overburden soil weight is reduced by the buoyancy force. Due to the
 385 assumptions that the cylinder is hollow instead of solid, and the vibration of the cylindrical
 386 foundations is not taken into account, the liquefaction criterion is (Jeng, 2013; Sumer, 2014):

$$(\gamma_s - \gamma_w)L_d \leq p_p - P_b \quad (19)$$

387 with γ_s and γ_w denoting seabed and water unit weight, respectively. In present study, $\gamma_s = 1.9 \gamma_w$
 388 is used to evaluate the weight of the overburden soil.

389

390 In this section, the development of liquefaction in the proximity of individual cylinders in an array is
 391 analysed for Case 2 with wave period $T = 10.5$ s (Table 3). The liquefaction depth has been evaluated
 392 using criterion (19). Results for each cylinder at the outer surface 0.1m away from the cylinder
 393 surface are shown in Figure 9 and Figure 10. In order to show the amplification of liquefaction
 394 induced by near-trapping phenomenon, the liquefaction depth (L_d) near a four-cylinder foundation is
 395 normalized by the single maximum liquefaction depth ($L_{d_{max}}^{MP}$) around a mono-pile foundation in the

396 entire liquefaction zone, i.e. within $-17.5\text{m} < x < 17.5\text{m}$ and $-17.5\text{m} < z < 17.5\text{m}$. The $L_{d_{max}}^{MP}$ values

397 of all the single cylinder cases from Table 3 are listed in Table 5. Figure 9(a) and (b) indicate that for
 398 0° wave heading there are two local minima of the liquefaction depth around both C1 and C2
 399 cylinders, occurring at θ equal 0° and 180° , and two local maxima, at θ equal 90° and 270° . Between
 400 these local minima and maxima liquefaction depth near the cylinder varies monotonically – it
 401 increases from $\theta=0^\circ$ to $\theta=90^\circ$, decreases from $\theta=90^\circ$ to $\theta=180^\circ$, and then repeats this cycle from $\theta=$
 402 180° to $\theta=360^\circ$. The liquefaction depth at the upstream end of cylinder, at $\theta=0^\circ$, is somewhat smaller

403 for C2, indicating a degree of sheltering by C1.

404

405

406 Table 5 the minimum free surface elevation (η_{\min}^{MP}), the minimum pore water pressure ($P_{b\min}^{\text{MP}}$) on the

407 seabed surface, and the maximum liquefaction depth ($L_{d\max}^{\text{MP}}$) around a mono-pile foundation

Case	1	2	3	4
η_{\min}^{MP} (m)	-2.84	-3.55	-4.97	-4.32
$P_{b\min}^{\text{MP}}$ (Pa)	-1.42×10^4	-1.90×10^4	-2.00×10^4	-2.40×10^4
$L_{d\max}^{\text{MP}}$ (m)	1.26	1.8	1.86	2

408

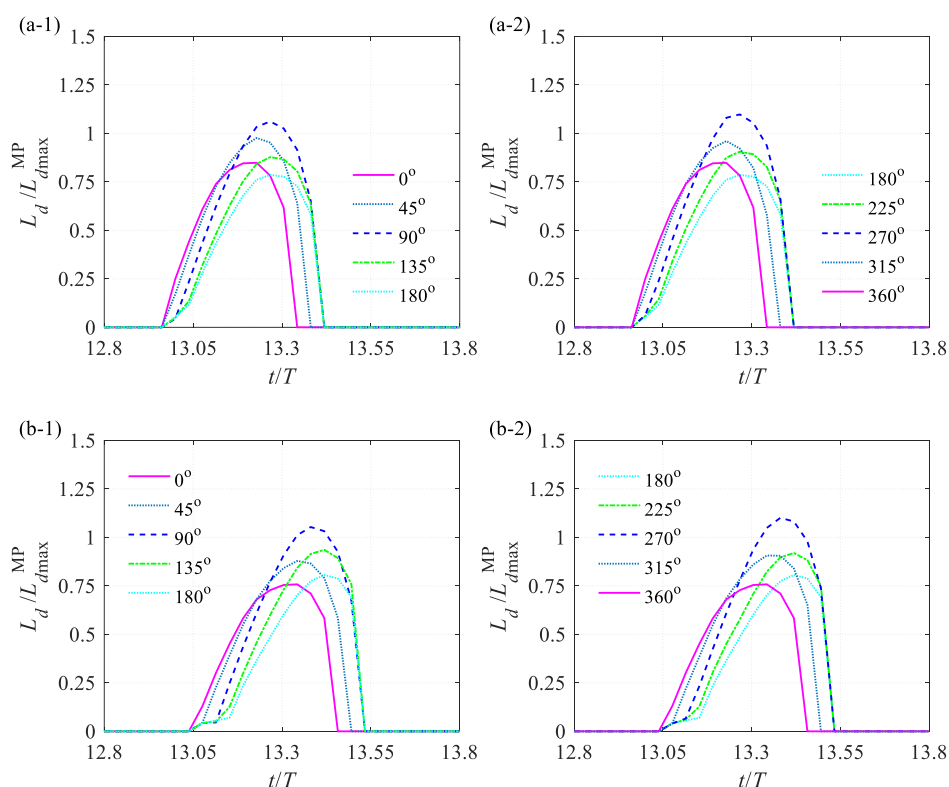


Figure 9 Development of liquefaction depth at various θ -locations with 0° incident wave. (a) C1 cylinder; (b) C2 cylinder. Refer to Figure 8 for the definition of θ , and to Figure 2 for the location of cylinders.

409

410 Development of liquefaction depth for 45° incident wave is shown in Figure 10. Owing to the

411 symmetry of liquefaction development along the lateral sides of C1 and C3 cylinders, results are

412 shown only for a half of their perimeter, from $\theta=0^\circ$ to $\theta=180^\circ$, in Figure 10(a) and (b), respectively.

413 For the same reason results are presented along the entire perimeter for C2, but not for C4, where

414 they are identical. The overall development of liquefaction depth around the perimeter of each
 415 individual cylinder is similar to that already seen for 0° heading wave. However, there is a notable
 416 difference between the values of the local minima of liquefaction depth at $\theta=0^\circ$ for cylinders C1 and
 417 C3 – the former is much deeper than the latter, leading to the conclusion that the upstream end of C3
 418 is protected by the three upstream cylinders. Comparison of the liquefaction development for groups
 419 of cylinders (Figure 9 and 10) with that for mono-pile (Figure 11) shows that the maximum
 420 momentary liquefaction depth in all cases takes place at $\theta=90^\circ$ and the magnitudes of liquefaction
 421 depth at all locations in both four-cylinder cases have been significantly amplified.
 422

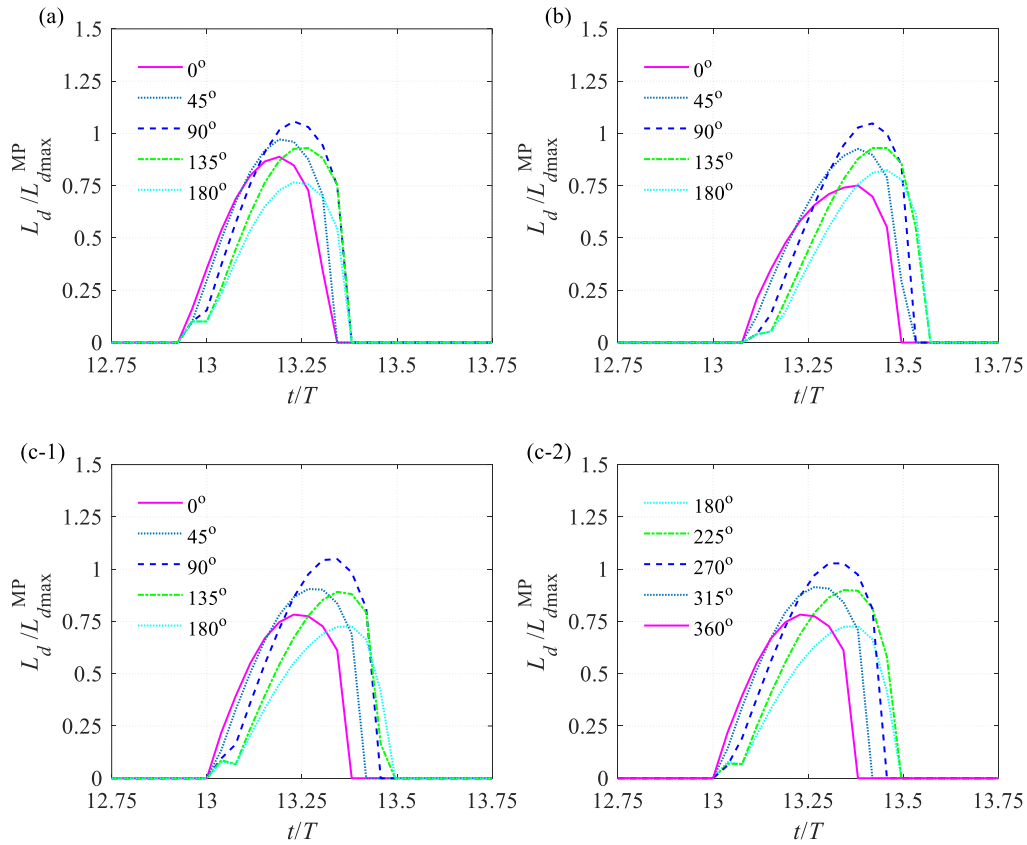


Figure 10 Development of liquefaction depth at various θ -locations with 45° incident wave. (a) C1 cylinder; (b) C3 cylinder; (c) C2 cylinder. Refer to Figure 8 for the definition of θ , and to Figure 3 for the location of cylinders.

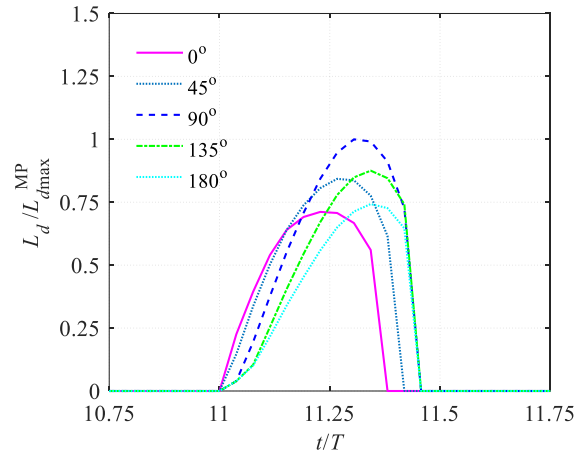


Figure 11 Development of liquefaction depth at various θ -locations with a mono-pile foundation. Refer to Figure 8 for the definition of θ .

423

424 4.2 Vertical distribution of pore water pressure around cylinders

425 For momentary liquefaction, the primary cause is attributed to the difference between the pore water
 426 pressure at seabed surface and a position beneath. As shown in section 4.1, the development of
 427 liquefaction depth around each cylinder in a cylinder array has been amplified by the near-trapping
 428 phenomenon of incident wave, which reduces the minimum free surface elevation during wave
 429 passage, and decreases the minimum wave-induced pressure at the seabed, resulting in deeper
 430 momentary liquefaction. In this section, in order to better understand the distribution of the
 431 maximum liquefaction depth around the perimeter of each cylinder, the liquefaction depth is
 432 estimated along an outer surface 0.1m away from cylinder surface at the moment when liquefaction
 433 depth reaches its maximum, such as $t/T= 13.3$ in Figure 9(a), and compared with those of a
 434 mono-pile foundation. Liquefaction depths are shown in Figures 12, 13, and 14 on the top of the
 435 contour plot of pore water pressure recorded at the same moment (p_p), normalized with the minimum
 436 pore water pressure (P_{bmin}^{MP} , listed in Table 5) on the seabed surface in a mono-pile foundation case.

437 The distribution of the liquefaction depth around the mono-pile perimeter is in qualitative agreement
 438 with experimental results of Tonkin et al. (2003), who also found the deepest scour at the cylinder
 439 side ($\theta=90^\circ$), albeit for tsunami waves rather than non-linear periodic waves used in the present
 440 study.

441

442 Figure 12 for 0° wave heading shows that the distributions of both pore water pressure and
 443 liquefaction depth around C1 and C2 cylinders are non-symmetric, unlike distributions along a
 444 mono-pile case foundation in Figure 13, which are symmetric with respect to $\theta=180^\circ$. A slightly
 445 non-symmetric distribution of liquefaction depth and pore water pressure near C2 cylinder is also
 446 indicated for 45° wave heading, in Figure 13(b), while these distributions near C1 and C3 cylinders
 447 are symmetric. For both 0° and 45° incident wave cases the inner zone ($180^\circ < \theta < 360^\circ$) towards the
 448 centre of the cylinder array shows more significant liquefaction than that of the outer zone
 449 ($0^\circ < \theta < 180^\circ$), away from the cylinder array centre. Moreover, the overall liquefaction depth and pore
 450 water pressure on seabed surface in the vicinity of each cylinder in a cylinder array are greater than

451 those around a mono-pile foundation. As stated earlier, this can be explained by the near-trapping
 452 phenomenon induced by wave-cylinders interaction above the seabed.

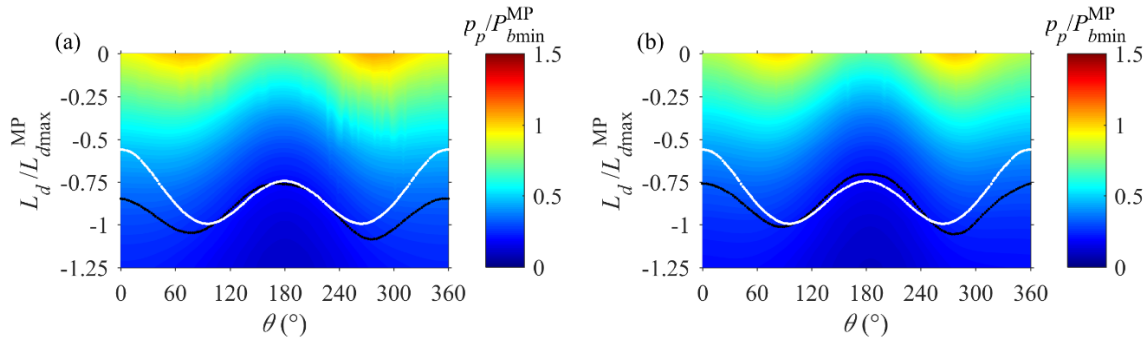


Figure 12 Pore water pressure and liquefaction depth for 0° incident wave along an outer surface at 0.1m distance from cylinder at the moment when the maximum liquefaction depth occurs. (a) C1 cylinder at $t/T=13.3$; (b) C2 cylinder at $t/T=13.4$. Black line shows liquefaction depth around individual cylinders in a cylinder array and white line shows liquefaction depth around mono-pile foundation. Refer to Figure 8 for the definition of θ , and to Figure 2 for the location of cylinders.

453

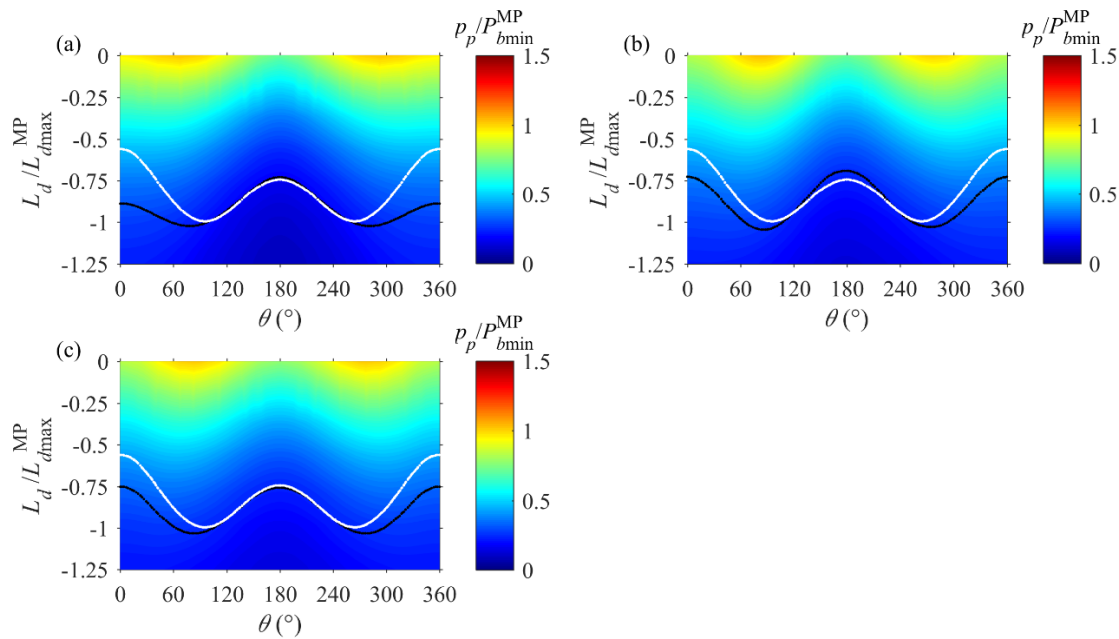


Figure 13 Pore water pressure and liquefaction depth for 45° incident wave along an outer surface at 0.1m distance from cylinder at the moment when the maximum liquefaction depth occurs. (a) C1 cylinder at $t/T=13.3$; (b) C2 cylinder at $t/T=13.37$; (c) C3 cylinder at $t/T=13.45$. Black line shows liquefaction depth around individual cylinders in a cylinder array and white line shows liquefaction depth around mono-pile foundation. Refer to Figure 8 for the definition of θ , and to Figure 3 for the location of cylinders.

454

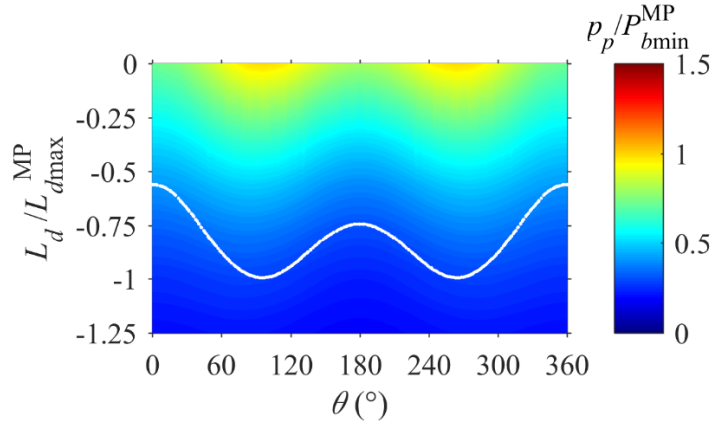


Figure 14 Pore water pressure and liquefaction depth along an outer surface at 0.1m distance from mono-pile foundation at the moment $t/T=11.35$ when the maximum liquefaction depth occurs. White line shows liquefaction depth around mono-pile foundation. Refer to Figure 8 for the definition of θ .

455

456 **4.3 Spatial distribution of the maximum values of liquefaction, pore water pressure on seabed** 457 **surface, and free surface elevation**

458 This section investigates the spatial distribution of the wave-induced liquefaction around individual
 459 cylinders in an array. Figure 15 shows the spatial distribution (in x - z plane) of the maximum
 460 liquefaction depth (L_d) within a wave period (calculated from stable results after 8 wave periods) for
 461 Case 1 to Case 4. As before the maximum liquefaction depth is normalized with the maximum
 462 liquefaction depth (L_{dmax}^{MP}) of a mono-pile foundation with the identical incoming wave. The

463 analogous post-processing is also applied to the minimum water pressure on the seabed surface (P_{bmin})
 464 and the minimum free surface elevation (η_{min}), and the associated results are shown in Figure 16 and
 465 Figure 17, respectively. Since liquefaction depth in the Case 5 with a mono-pile foundation is small,
 466 the discussion of this case will be presented later, in section 4.5.

467

468 Comparison of the normalized maximum liquefaction depths for 0° and 45° incident waves with
 469 those for a mono-pile foundation case (Figure 15) shows that the amplification factors for the
 470 maximum liquefaction depth range approximately from 1.05 to 1.2. Moreover, under the action of 0°
 471 incident wave amplification of liquefaction depth is more noticeable (Figure 15a), then for 45°
 472 incident wave (Figure 15b), especially at the lateral sides of front cylinders (C1 and C4 for 0°
 473 incident wave, and C1 for 45° incident wave). The maximum momentary liquefaction zones are
 474 located at the lateral sides of individual cylinders, and between the two front cylinders (C1 and C4)
 475 for 0° incident wave. This agrees with Cong et al. (2015) who concluded that the amount of
 476 incoming wave is trapped in the zone between C1 and C4 and the inner zone of a four-cylinder
 477 structure is shielded without significant amplification. At the lateral sides of cylinders in Figure 15(a),
 478 the decrease of $k_w D$ from 0.35 (shorter wave) to 0.25 (longer wave) leads to the more significant
 479 amplification on liquefaction depth, but for $k_w D$ of 0.2 (Case 4) the amplification factor reduces to
 480 approximately 1.05. A possible explanation is that due to the greater wave length in Case 4 the
 481 four-cylinder group behaves as a unity. The distribution of liquefaction around a cylinder group is

482 therefore similar to that around a mono-pile foundation, where the smaller liquefaction depth is also
483 shown in front of the cylinder array.

484

485 Figure 16 shows the spatial distribution of the minimum wave-induced pressure on seabed surface,
486 P_b . It is very similar to the distribution of the maximum liquefaction depth shown in Figure 15,
487 indicating that reduction of P_b is the primary cause of the momentary liquefaction. The minimum
488 seabed pressure P_b is in turn associated with the minimum free surface elevation, shown in Figure 17.
489 However, although their general distribution is similar, free surface elevation seems to be more
490 violent and contains higher-order harmonic components (Readers are referred to the Fig.8 and Fig.9
491 in Lin et al. (2017) for the temporal comparisons of these three variables). This is because wave
492 pressure attenuation with water depth is frequency dependent, so the attenuation of wave pressure for
493 higher harmonic components is faster than that for lower frequency harmonics, hence higher order
494 harmonic components attenuate between the water surface and the seabed surface and do not reach
495 the latter. Consequently the near-trapping phenomenon of wave-induced pressure on seabed surface
496 and the resulting momentary liquefaction are somewhat different from that of free surface elevation,
497 which contains higher-order harmonic components. The spatial distribution of the minimum free
498 surface elevation (η_{\min}) in Figure 17 further confirms that the incident wave though trapped inside the
499 cylinder array causes lower water levels within the inner zone compared with those outside.

500

501 To demonstrate the overall effect of the near-trapping on a cylinder group, and compare it with a
502 mono-pile, the amplification factors averaged over the previously defined liquefaction zone (-17.5m
503 $< x < 17.5\text{m}$ and $-17.5\text{m} < z < 17.5\text{m}$) are shown in Figure 18, together with the minimum and the
504 maximum amplification factors. It can be seen that the average amplification factor does not linearly
505 increase with the decrease of $k_w D$ and the increase of wave period. The sudden increase of
506 amplification factor at $k_w D = 0.25$ ($T = 12.05\text{s}$) is also confirmed by both experimental results and
507 numerical simulation in Cong et al. (2015) for investigating the effect of near-trapping phenomenon,
508 but the overall development of amplification factors tends to stabilize with the increase of wave
509 period. It can be noticed that the developments of amplification factor with $k_w D$ for liquefaction
510 depth, wave pressure on seabed surface, and free surface elevation, follow similar patterns. Moreover,
511 the amplification factors for liquefaction depth and wave pressure on seabed surface are similar,
512 while the effect of the near-trapping phenomenon on free surface elevation is more pronounced. The
513 incident wave for two different incident angles are found to be trapped in a four cylinder structure,
514 and result in the noticeable amplification factor compared to that of a mono-pile case. For the
515 incoming wave angles, it can be seen that the incident wave with 0° heading seems to be trapped
516 easier than that of 45° headings and mono-pile case, leading to greater amplification factors.

517

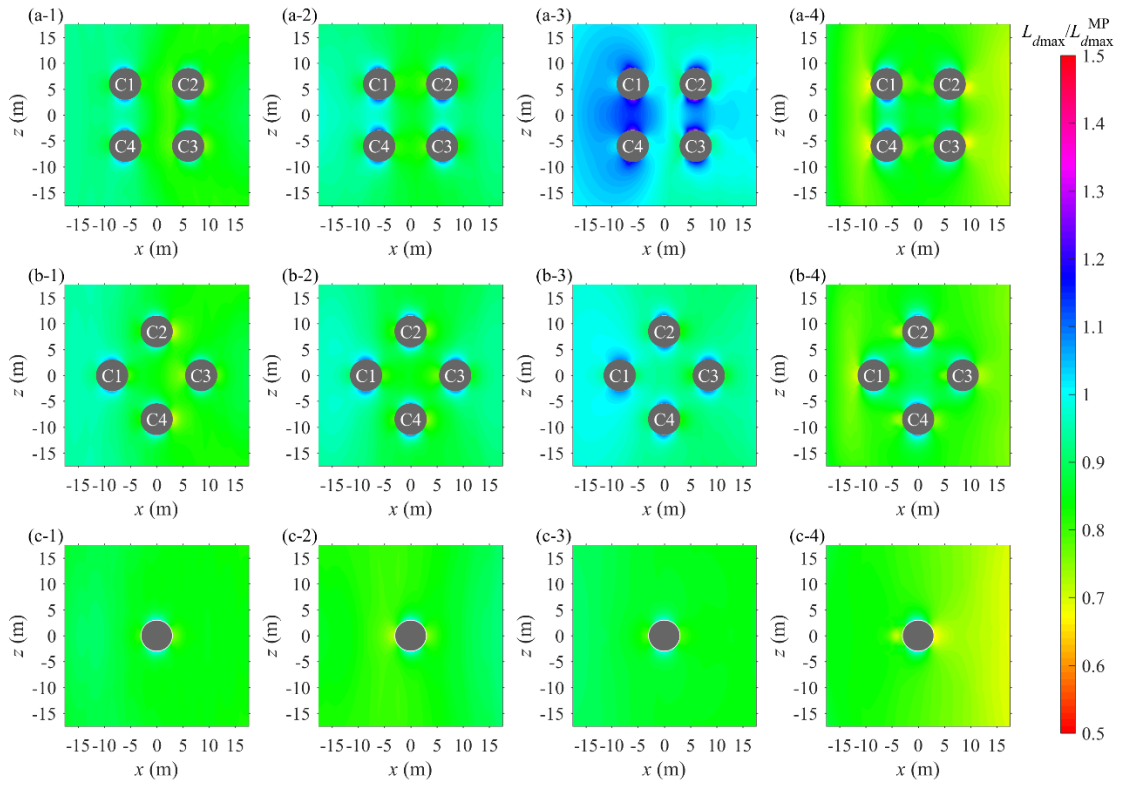


Figure 15 Spatial distribution of the normalized maximum liquefaction depth (L_{dmax}) within a wave period over the maximum liquefaction depth (L_{dmax}^{MP}) in the mono-pile case with same incident wave. (a) 0° incident wave; (b) 45° incident wave; (c) a mono-pile case. The numbering indicates the case number in Table 3.

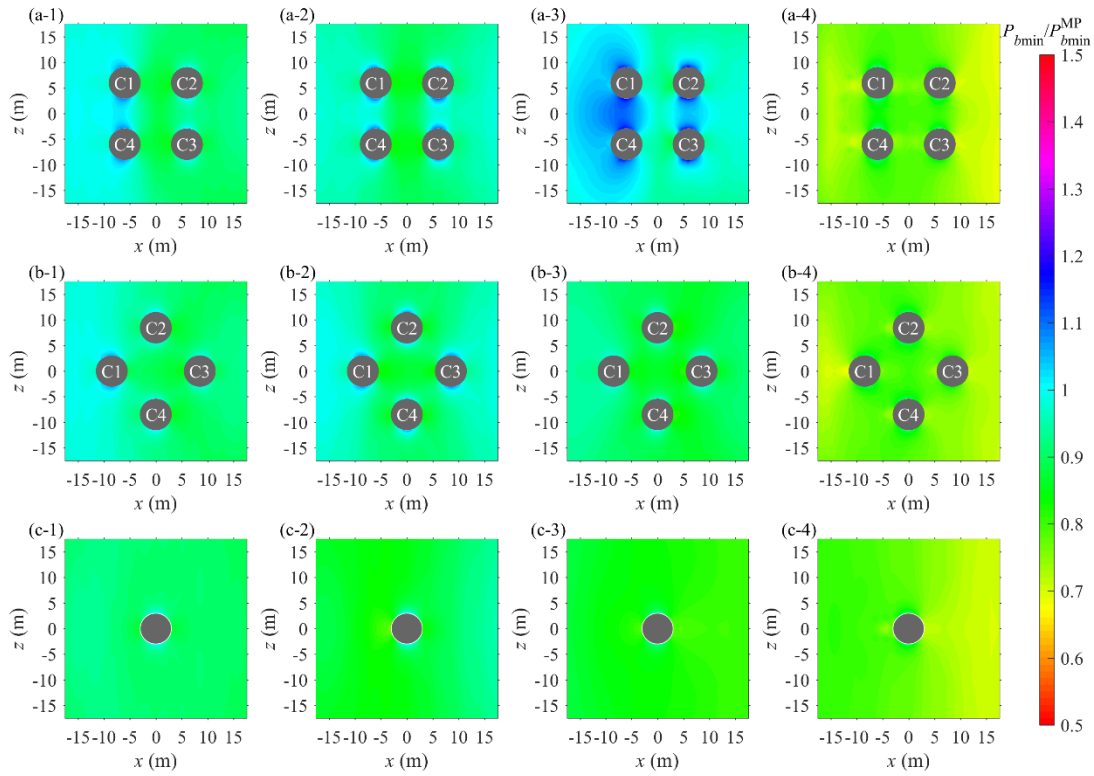


Figure 16 Spatial distribution of the normalized minimum pore water pressure at seabed (P_{bmin}) within a wave period over the minimum pore water pressure (P_{bmin}^{MP}) in the mono-pile case with same incident wave. (a) 0° incident wave; (b) 45° incident wave; (c) a mono-pile case. The numbering indicates the case number in Table 3.

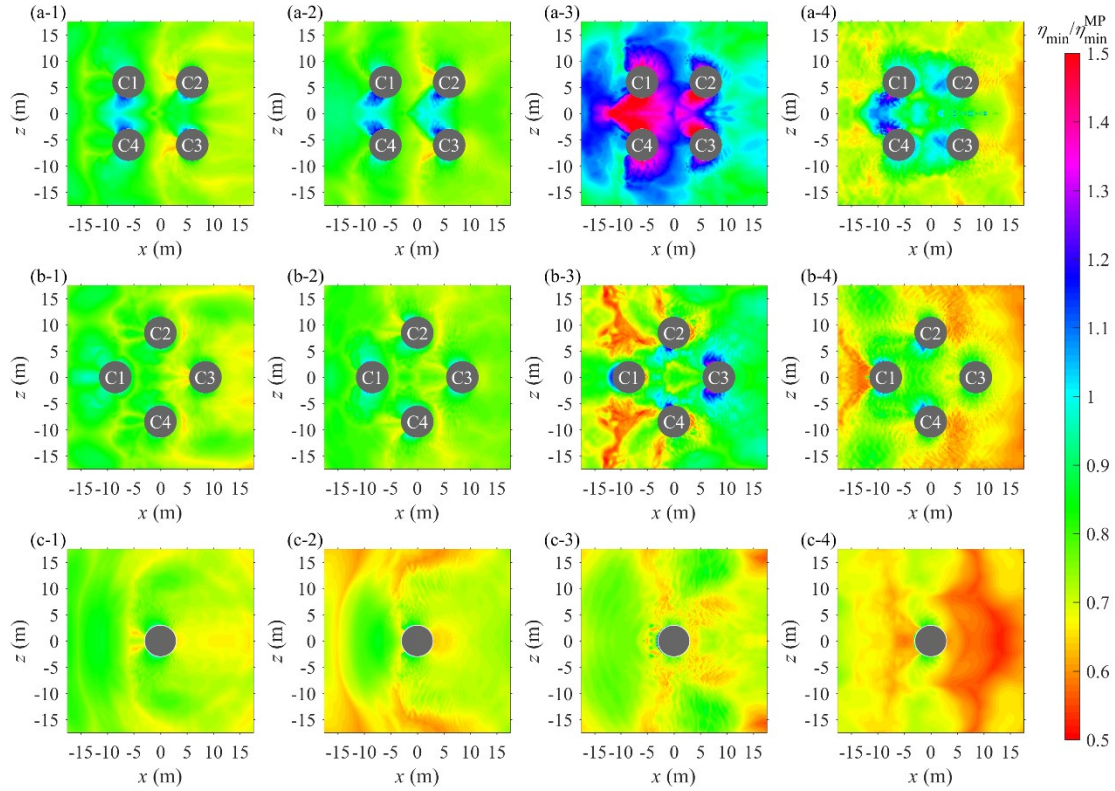


Figure 17 Spatial distribution of the normalized minimum free surface elevation (η_{\min}) within a wave period over the minimum free surface elevation (η_{\min}^{MP}) in the mono-pile case with same incident wave. (a) 0° incident wave; (b) 45° incident wave; (c) a mono-pile case. The numbering indicates the case number in Table 3.

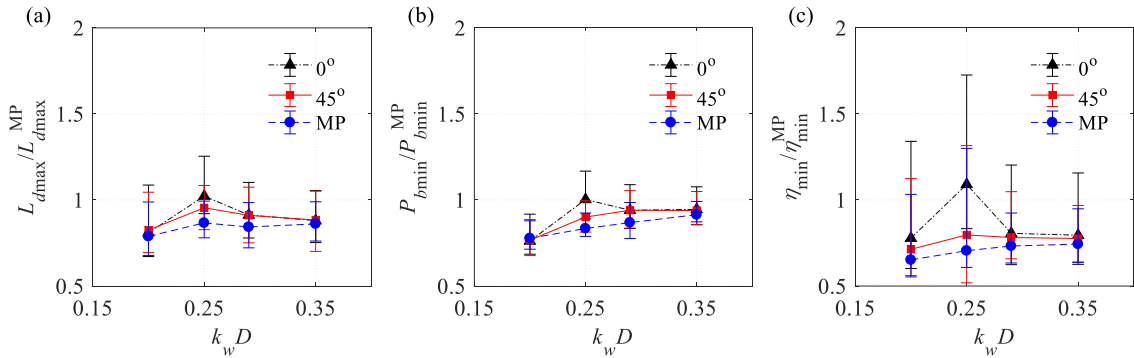


Figure 18 Average, the minimum, and the maximum amplification factors for different layouts and $k_w D$; (a) liquefaction depth L_d ; (b) seabed surface pressure P_b ; (c) free surface elevation η .

520

521 4.4 Influence of incident angle

522 For a better understanding of how the maximum liquefaction depth is distributed around each
 523 cylinder surface, the maximum liquefaction across the same vertical circular plane as in Figure 9 and
 524 Figure 10 for two incident wave angles are compared with the result of a single cylinder case (Figure
 525 11) and presented in Figure 19. Good protection effect of the upstream cylinder (C1) on the vicinity
 526 of the front (0°) and back (180°) of downstream cylinder (C2 with 0° wave heading and C3 with 45°

527 wave heading) can be confirmed in all cases with both incident angles. A special attention needs to
 528 be paid to the back side of each downstream cylinder, where the maximum momentary liquefaction
 529 depth is smaller than that at the back side of upstream cylinder. This can also be attributed to the
 530 protection effect from front cylinders. Comparing the liquefaction depth around individual cylinders
 531 in an array with the result of a mono-pile foundation case, it is evident that the liquefaction depth
 532 with a four-cylinder foundation is overall greater, and the upstream cylinder(s) experience more
 533 significant liquefaction threat than other cylinders in an array.

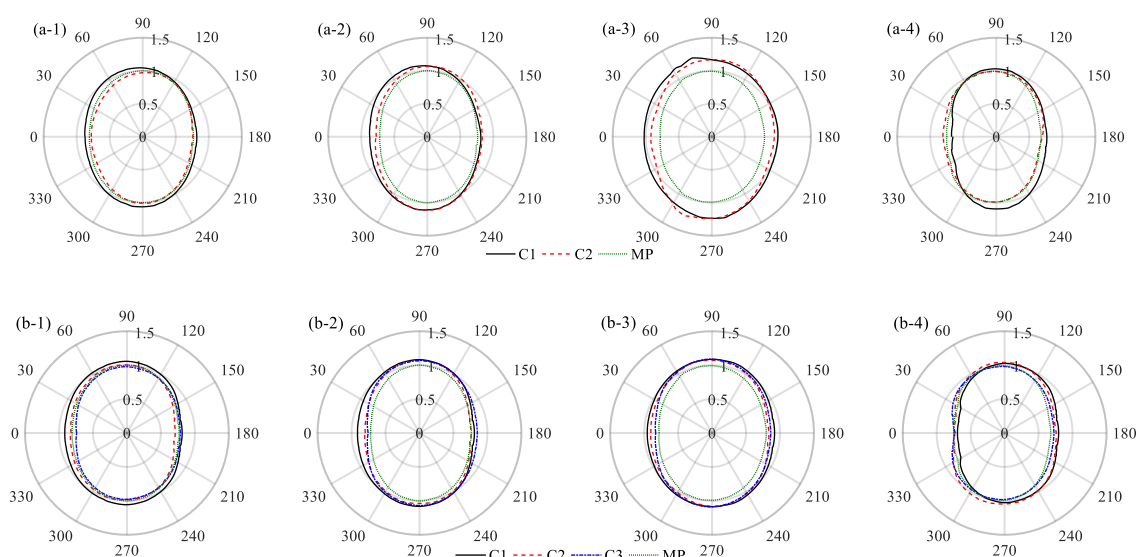


Figure 19 Polar plot of the normalized of the maximum liquefaction depth (L_{dmin}) within a wave period over the maximum liquefaction depth (L_{dmax}^{MP}) in the mono-pile case with same incident wave. (a) 0° incident wave; (b) 45° incident wave. Refer to Figure 8 for the definition of θ , and to Figure 2 for the location of cylinders. The numbering indicates the case number in Table 3.

534
 535 On the basis of the spatial distribution of wave-induced pressure on seabed surface in Figure 16, the
 536 minimum value is located at the lateral sides of each cylinder. For momentary liquefaction, the
 537 primary cause is the wave-induced pressure under wave trough. Therefore, the maximum momentary
 538 liquefaction is distributed at both lateral sides of each circular cylinder. Figure 19 further confirms
 539 this: the maximum liquefaction depth over a wave period indeed takes place at both lateral sides of
 540 each cylinder. Moreover, for 0° incident wave (Figure 19a) the distribution of the maximum
 541 liquefaction depth in the vicinity of both upstream and downstream cylinders (C1 and C2) is
 542 non-symmetric. In contrast, Figure 19(b) shows that for 45° incident wave the distribution of the
 543 maximum liquefaction depth in the vicinity of the lateral cylinder C2 is fairly symmetric.

544 545 **4.5 Liquefaction around foundation under shorter waves**

546 As aforementioned in section 4.3, the liquefaction depth near a mono-pile foundation in Case 5
 547 (Table 3) is small, so this case is now discussed separately from other four cases. The maximum
 548 liquefaction depth over a wave period in Case 5 is presented in Figure 20, where in both incident
 549 wave directions liquefaction is most pronounced in front of a cylinder array and liquefaction depth at

550 the back of a cylinder array is smaller. This further confirms the good protection of downstream
 551 cylinders by upstream cylinders, which was discussed in sections 4.3 and 4.4: the upstream cylinders
 552 (C1 and C4 with 0° wave heading; C1 with 45° wave heading) may encounter more significant
 553 liquefaction threat than the downstream cylinders. Regarding the mono-pile foundation, shorter
 554 incident wave generates much smaller liquefaction depth in the vicinity of the cylinder.

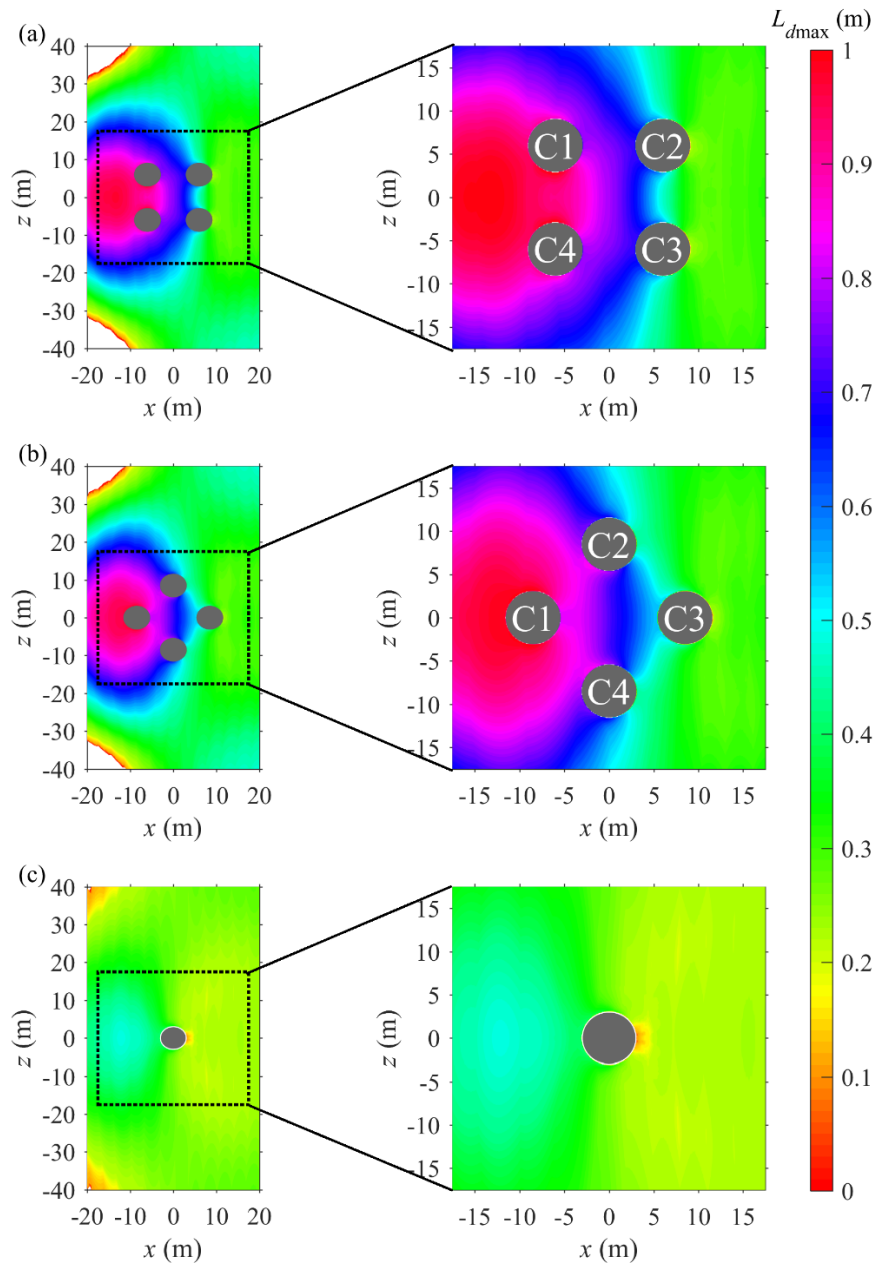


Figure 20 Spatial distribution of the maximum liquefaction depth with (a) 0° incident wave, (b) 45° incident wave, and (c) a mono-pile foundation.

555
 556 As before, spatial distributions of liquefaction depth are compared with the spatial distribution of the
 557 normalized the minimum wave-induced pressure on seabed surface and free surface elevation shown
 558 in Figure 21. Spatial distributions of liquefaction depth and the seabed pressure are almost identical,
 559 whereas the spatial distribution of the minimum free surface elevation is similar to them, especially

560 in the region near the front cylinders, but also contains higher order harmonics absent from other two.
 561 In addition, the normalized minimum wave-induced pressure on seabed surface shown in Figure
 562 21(a), indicates that the approximate range of the amplification factor, resulting from near-trapping
 563 phenomenon of incoming wave within a cylinder array, is from 1.1 to 1.4. With shorter incident wave
 564 (Case 5 with $k_w D = 0.43$), the near-trapping effect tends to be more significant, with greater
 565 amplification factor, while the liquefaction depth, compared to longer wave (Case 1 with $k_w D = 0.35$
 566 and L_d of roughly 1.38m), is smaller, roughly 1m, due to the smaller magnitude of wave-induced
 567 pressure under wave trough. Nevertheless, the soil response near a cylinder array under such shorter
 568 waves should still be examined in terms of liquefaction potential, especially for cylinder arrays
 569 where the near-trapping phenomenon is capable of reducing the minimum wave-generated pressure
 570 at seabed, compared to a single cylinder.

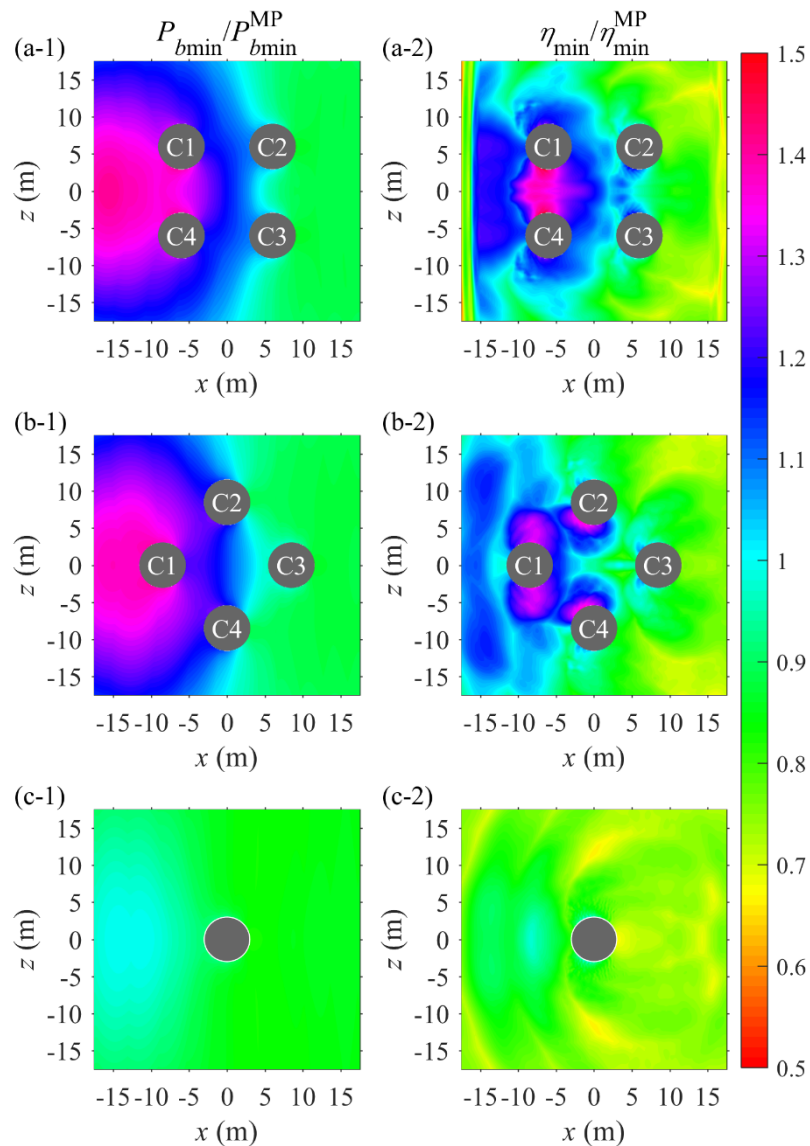


Figure 21 Spatial distribution of the normalized minimum wave-induced pressure (P_{bmin} ; see subplots a-1, b-1, c-1) on seabed surface and free surface elevation (η_{min} ; see subplots a-2, b-2, c-2) in a wave period. (a) 0° incident wave; (b) 45° incident wave; (c) a mono-pile foundation.

572 **5. Conclusions**

573 Previous study (Lin et al., 2017) demonstrated that the presence of mono-pile foundation has
574 significant effect on the distribution of wave-induced pore water pressures and associated potential
575 liquefaction. Nevertheless, the understanding of the liquefaction potential around a cylinder array
576 under storm wave remains an unsolved issue. With the WSSI model proposed in Lin et al. (2017), an
577 investigation of wave-induced seabed response and liquefaction potential in the vicinity of closely
578 placed four cylinders has been carried out, for two incident wave angles, namely 0° and 45° , and for
579 a range of wave conditions. The following conclusions can be drawn from this study:

580

581 (1) The capability of present wave model to simulate wave-cylinders interaction has been
582 demonstrated. It shows that good accuracy can be obtained, even for higher order components,
583 and for the steep wave. This agrees with the conclusion drawn in Sun et al. (2016) for single
584 cylinder case. This study extends this conclusion to cylinder arrays. The near-trapping
585 phenomenon is well captured and the wave sub-model in the coupled WSSI model is capable of
586 simulating wave-cylinders interaction.

587 (2) The magnitudes of wave-induced free surface elevation and pressure in the vicinity of a cylinder
588 array, as well as associated liquefaction depth, are amplified by the near-trapping phenomenon
589 occurring during interaction of wave with an array of cylinders. Compared with the results of a
590 mono-pile foundation case under same wave parameters, the amplification factor for liquefaction
591 depth, wave-induced pressure, and free surface elevation is approximately in the range from 1.05
592 to 1.2. In general, the amplification factor decreases with the increase of wave period. This is
593 also demonstrated in Cong et al. (2015) by experimental and numerical investigations of free
594 surface elevation. Although the numerical results of soil model are highly sensitive to the soil
595 parameters used in the study, the overall phenomenon of soil response under near-trapping
596 effects can still be captured as wave-induced pore pressures within the seabed are well predicted
597 numerically and irrelevant to soil parameters. The potential for liquefaction needs to be
598 examined even in the case with shorter wave and smaller wave height, in which no liquefaction
599 takes place around the mono-pile foundation, but may still happen near a cylinder array, due to
600 the effect of near-trapping phenomenon.

601 (3) The overall liquefaction depth near a four-cylinder group under 0° incident wave is greater than
602 that under 45° incident wave. This is because the wave with 0° incident direction has significant
603 near-trapping phenomenon inside the cylinder array, which leads to smaller seabed pore pressure
604 than for 45° incident wave. As a result, the porous seabed at the inner zone of a four-cylinder
605 array is more vulnerable to liquefaction threat than that at the outer zone in both incident wave
606 directions since lower wave-induced pressures occur in this zone. Non-symmetric spatial
607 distributions of wave-induced pressure, liquefaction depth, and the minimum free surface
608 elevation are found under 0° wave heading, while those under 45° wave heading are symmetric.

609 (4) In a four-cylinder array, upstream cylinders provide good protection from momentary
610 liquefaction for downstream cylinders. As before, this directly corresponds to the spatial
611 distribution of the minimum wave-induced pressure on seabed around cylinders. Furthermore,
612 the momentary liquefaction depth is largest at the lateral sides of each cylinder. Good protection
613 from momentary liquefaction therefore needs to be placed in these zones.

614 **Acknowledgement**

615 The authors would like to acknowledge the financial support from Energy Technology Partnership
 616 (ETP), Wood Group Kenny, and University of Aberdeen. Zaibin Lin greatly appreciates the helpful
 617 discussion with Dr Dominic van der A from the University of Aberdeen. The constructive comments
 618 from Prof. Dong-Sheng Jeng at Griffith University have greatly improved the quality of the
 619 manuscript.

620

621 **Nomenclature**

A	Wave amplitude	[m]
D	Diameter of pipeline or cylinder	[m]
e	Penetration depth	[m]
E	Young's modulus	[MPa]
\mathbf{g}	Gravitational acceleration vector	[m/s ²]
G	Shear modulus of soil	[N/m ²]
h_s	Soil depth	[m]
h_w	Mean water level or water depth	[m]
H_w	Wave height	[m]
k_s	Darcy's permeability	[m/s]
k_w	Wave number	[m ⁻¹]
K_0	Coefficient of earth pressure at rest	[-]
K_w	True bulk modulus of elasticity of water	[N/m ²]
L_d	Liquefaction depth	[m]
L_{dmax}^{MP}	The maximum liquefaction depth of a mono-pile foundation	[m]
L_s	Soil domain length	[m]
L_w	Wave length	[m]
\mathbf{n}	The normal to the body surface	[-]
n_s	Porosity of soil	[-]
p	Total pressure	[kPa]
P_{bmin}^{MP}	The minimum pore water pressure on the seabed surface in a mono-pile foundation case	[kPa]

p_p	Pore water pressure	[kPa]
p_w	Hydrostatic water pressure	[kPa]
P_0	The maximum pore water pressure	[kPa]
P_b	Pore water pressure on the seabed surface	[kPa]
P_{w0}	Absolute pore water pressure	[kPa]
S_r	Saturation degree of soil	[-]
t	Time	[s]
T	Wave period	[s]
\mathbf{u}	Velocity field	[m/s]
\mathbf{u}_a	Air velocity	[m/s]
\mathbf{u}_r	Relative velocity field	[m/s]
\mathbf{u}^T	Transpose matrix of velocity field	[m/s]
\mathbf{u}_w	Water velocity	[m/s]
\mathbf{v}	$\mathbf{v} = (u_s, v_s, w_s)$, the vector of soil displacement	[m]
\mathbf{x}	$\mathbf{x} = (x, y, z)$, Cartesian coordinate vector where y is the vertical coordinate, x and z are the horizontal coordinates.	[m]
W_s	Soil domain width	[m]
α	Volume fraction function	[-]
β_s	Compressibility of pore fluid	[m ² /N]
γ_s	Unit weight of soil	[kN/m ³]
γ_w	Unit weight of water	[kN/m ³]
ε_s	Volume strain	[-]
η	Free surface elevation	[m]
η_{\min}	The minimum free surface elevation	[m]
η_{\min}^{MP}	The minimum free surface elevation in the mono-pile case	[m]
θ	Angle along circular cylinder circumference	[°]
θ_w	Wave direction	[°]

μ	Dynamic viscosity	[kg/sm]
μ_w	Dynamic viscosity of water	[kg/sm]
μ_a	Dynamic viscosity of air	[kg/sm]
ν	Poisson's ratio	[-]
ρ	Fluid density	[kg/m ³]
ρ_w	Water density	[kg/m ³]
ρ_a	Air density	[kg/m ³]
σ_{ij}	The rate of the strain tensor	[-]
σ'	Effective normal stress	[kPa]
τ	Shear stress	[kPa]
ω	Frequency of incident wave	[s ⁻¹]

622

623

624

625

626 **References**

627 Berberović, E., van Hinsberg, N.P., Jakirlić, S., Roisman, I.V. and Tropea, C., 2009. Drop impact
628 onto a liquid layer of finite thickness: Dynamics of the cavity evolution. *Physical Review E*,
629 79(3): 036306.

630 Bihs, H., Kamath, A., Alagan Chella, M. and Arntsen, Ø.A., 2016. Breaking-Wave Interaction with
631 Tandem Cylinders under Different Impact Scenarios. *Journal of Waterway, Port, Coastal,
632 and Ocean Engineering, ASCE*: 04016005.

633 Biot, M.A., 1941. General theory of three-dimensional consolidation. *Journal of Applied Physics*,
634 12(2): 155-164.

635 Chang, K.-T. and Jeng, D.-S., 2014. Numerical study for wave-induced seabed response around
636 offshore wind turbine foundation in Donghai offshore wind farm, Shanghai, China. *Ocean
637 Engineering*, 85: 32-43.

638 Chen, L., Zang, J., Hillis, A., Morgan, G. and Plummer, A., 2014. Numerical investigation of
639 wave–structure interaction using OpenFOAM. *Ocean Engineering*, 88: 91-109.

640 Cong, P., Gou, Y., Teng, B., Zhang, K. and Huang, Y., 2015. Model experiments on wave elevation
641 around a four-cylinder structure. *Ocean Engineering*, 96: 40-55.

642 Duan, L. and Jeng, D.-S., 2018. Numerical studies for wave-induced pore-water pressures around
643 group of piled foundations. *The 28th ISOPE International Ocean and Polar Engineering
644 Conference*, Sapporo, Hokkaido, Japan, June 10-15, 2018 (CD-ROM).

645 Duan, L., Jeng, D.S. and Wang, D., 2019. PORO-FSSI-FOAM: Seabed response around a mono-pile
646 under natural loadings. *Ocean Engineering*, 184: 239-254.

647 Engsig-Karup, A.P., Bingham, H.B. and Lindberg, O., 2009. An efficient flexible-order model for 3D

648 nonlinear water waves. *Journal of computational physics*, 228(6): 2100-2118.

649 Higuera, P., Lara, J.L. and Losada, I.J., 2013a. Realistic wave generation and active wave absorption
650 for Navier–Stokes models: Application to OpenFOAM®. *Coastal Engineering*, 71: 102-118.

651 Higuera, P., Lara, J.L. and Losada, I.J., 2013b. Simulating coastal engineering processes with
652 OpenFOAM®. *Coastal Engineering*, 71: 119-134.

653 Higuera, P., Lara, J.L. and Losada, I.J., 2014a. Three-dimensional interaction of waves and porous
654 coastal structures using OpenFOAM®. Part I: Formulation and validation. *Coastal
655 Engineering*, 83: 243-258.

656 Higuera, P., Lara, J.L. and Losada, I.J., 2014b. Three-dimensional interaction of waves and porous
657 coastal structures using OpenFOAM®. Part II: Application. *Coastal Engineering*, 83:
658 259-270.

659 Higuera, P., Losada, I.J. and Lara, J.L., 2015. Three-dimensional numerical wave generation with
660 moving boundaries. *Coastal Engineering*, 101: 35-47.

661 Hirt, C.W. and Nichols, B.D., 1981. Volume of fluid (VOF) method for the dynamics of free
662 boundaries. *Journal of computational physics*, 39(1): 201-225.

663 Jacobsen, N.G., Fuhrman, D.R. and Fredsøe, J., 2012. A wave generation toolbox for the open-source
664 CFD library: OpenFoam®. *International Journal for Numerical Methods in Fluids*, 70(9):
665 1073-1088.

666 Jeng, D.-S., 2003. Wave-induced sea floor dynamics. *Applied Mechanics Reviews*, 56(4): 407-429.

667 Jeng, D.-S., 2013. Porous Models for Wave-seabed Interactions. *Springer Berlin Heidelberg*.

668 Jeng, D.-S. and Cha, D.H., 2003. Effects of dynamic soil behavior and wave non-linearity on the
669 wave-induced pore pressure and effective stresses in porous seabed. *Ocean Engineering*,
670 30(16): 2065-2089.

671 Jeng, D.-S., Ye, J.H., Zhang, J.S. and Liu, P.L.F., 2013. An integrated model for the wave-induced
672 seabed response around marine structures: Model verifications and applications. *Coastal
673 Engineering*, 72(0): 1-19.

674 Jeng, D.S., 2018. Mechanics of Wave-seabed-structure Interactions: Modelling, Processes and
675 Applications. *Cambridge University Press*.

676 Kamath, A., Bihs, H., Alagan Chella, M. and Arntsen, Ø.A., 2016. Upstream-cylinder and
677 downstream-cylinder influence on the hydrodynamics of a four-cylinder group. *Journal of
678 Waterway, Port, Coastal, and Ocean Engineering*, ASCE: 04016002.

679 Kamath, A., Chella, M.A., Bihs, H. and Arntsen, Ø.A., 2015. CFD investigations of wave interaction
680 with a pair of large tandem cylinders. *Ocean Engineering*, 108: 738-748.

681 Kirby, J., Wen, L. and Shi, F., 2003. Funwave 2.0 fully nonlinear boussinesq wave model on
682 curvilinear coordinates. *Center for Applied Coastal Research Dept. of Civil & Environmental
683 Engineering, University of Delaware, Newark*.

684 Li, X.-J., Gao, F.-P., Yang, B. and Zang, J., 2011. Wave-induced pore pressure responses and soil
685 liquefaction around pile foundation. *International Journal of Offshore and Polar Engineering*,
686 21(03).

687 Li, Y., Ong, M.C. and Tang, T., 2018. Numerical analysis of wave-induced poro-elastic seabed
688 response around a hexagonal gravity-based offshore foundation. *Coastal Engineering*, 136:
689 81-95.

690 Liao, C., Jeng, D.-S. and Zhang, L., 2013. An analytical approximation for dynamic soil response of
691 a porous seabed due to combined wave and current loading. *Journal of Coastal Research*,
692 31(5): 1120-1128.

693 Lin, Z., Guo, Y., Jeng, D.-S., Liao, C. and Rey, N., 2016. An integrated numerical model for
694 wave–soil–pipeline interactions. *Coastal Engineering*, 108: 25-35.

695 Lin, Z., Pokrajac, D., Guo, Y., Jeng, D.-S., Tang, T., Rey, N., Zheng, J. and Zhang, J., 2017.
696 Investigation of nonlinear wave-induced seabed response around mono-pile foundation.
697 *Coastal Engineering*, 121: 197-211.

698 Linton, C. and Evans, D., 1990. The interaction of waves with arrays of vertical circular cylinders.
699 *Journal of fluid mechanics*, 215: 549-569.

700 Liu, B., Jeng, D.-S., Ye, G. and Yang, B., 2015. Laboratory study for pore pressures in sandy deposit
701 under wave loading. *Ocean Engineering*, 106: 207-219.

702 Liu, X., García, M.H. and Muscari, R., 2007. Numerical investigation of seabed response under
703 waves with free-surface water flow. *International Journal of Offshore and Polar Engineering*,
704 17(02).

705 Malenica, Š., Eatock Taylor, R. and Huang, J., 1999. Second-order water wave diffraction by an
706 array of vertical cylinders. *Journal of Fluid Mechanics*, 390: 349-373.

707 Ohl, C., Eatock Taylor, R., Taylor, P. and Borthwick, A., 2001a. Water wave diffraction by a cylinder
708 array. Part 1. Regular waves. *Journal of Fluid Mechanics*, 442: 1-32.

709 Ohl, C., Taylor, P., Eatock Taylor, R. and Borthwick, A., 2001b. Water wave diffraction by a cylinder
710 array. Part 2. Irregular waves. *Journal of Fluid Mechanics*, 442: 33-66.

711 Paulsen, B.T., Bredmose, H. and Bingham, H.B., 2014a. An efficient domain decomposition strategy
712 for wave loads on surface piercing circular cylinders. *Coastal Engineering*, 86: 57-76.

713 Paulsen, B.T., Bredmose, H., Bingham, H.B. and Jacobsen, N.G., 2014b. Forcing of a
714 bottom-mounted circular cylinder by steep regular water waves at finite depth. *Journal of*
715 *Fluid Mechanics*, 755: 1-34.

716 Qi, W.-G. and Gao, F.-P., 2014. Physical modeling of local scour development around a
717 large-diameter monopile in combined waves and current. *Coastal Engineering*, 83: 72-81.

718 Shi, F., Dalrymple, R.A., Kirby, J.T., Chen, Q. and Kennedy, A., 2001. A fully nonlinear Boussinesq
719 model in generalized curvilinear coordinates. *Coastal Engineering*, 42(4): 337-358.

720 Spring, B.H. and Monkmeyer, P.L., 1974. Interaction of plane waves with vertical cylinders.
721 *Proceedings of the 14th international conference on coastal engineering*.

722 Sui, T., Zhang, C., Guo, Y., Zheng, J., Jeng, D.-S., Zhang, J. and Zhang, W., 2016. Three-dimensional
723 numerical model for wave-induced seabed response around mono-pile. *Ships and Offshore*
724 *Structures*: 1-12.

725 Sui, T., Zhang, C., Jeng, D.-s., Guo, Y., Zheng, J., Zhang, W. and Shi, J., 2019. Wave-induced seabed
726 residual response and liquefaction around a mono-pile foundation with various embedded
727 depth. *Ocean Engineering*, 173: 157-173.

728 Sui, T., Zheng, J., Zhang, C., Jeng, D.-S., Zhang, J., Guo, Y. and He, R., 2017. Consolidation of
729 unsaturated seabed around an inserted pile foundation and its effects on the wave-induced
730 momentary liquefaction. *Ocean Engineering*, 131: 308-321.

731 Sumer, B.M., 2014. Liquefaction Around Marine Structures. *World scientific, New Jersey*.

- 732 Sumer, B.M. and Fredsøe, J., 2002. The mechanics of scour in the marine environment. *World*
733 *Scientific, New Jersey*.
- 734 Sun, K., Zhang, J., Gao, Y., Jeng, D.-s., Guo, Y. and Liang, Z., 2019. Laboratory experimental study
735 of ocean waves propagating over a partially buried pipeline in a trench layer. *Ocean*
736 *Engineering*, 173: 617-627.
- 737 Sun, L., Zang, J., Chen, L., Eatock Taylor, R. and Taylor, P., 2016. Regular waves onto a truncated
738 circular column: A comparison of experiments and simulations. *Applied Ocean Research*, 59:
739 650-662.
- 740 Tang, T., 2014. Modeling of soil-water-structure interaction: A Finite Volume Method (FVM)
741 approach to fully coupled soil analysis and interactions between wave, seabed and offshore
742 structure. PhD thesis, Technical University of Denmark.
- 743 Tang, T. and Hededal, O., 2014. Simulation of pore pressure accumulation under cyclic loading using
744 Finite Volume Method. *Proceedings of 8th European Conference on Numerical Methods in*
745 *Geotechnical Engineering (numge14)*.
- 746 Tang, T., Hededal, O. and Cardiff, P., 2015. On finite volume method implementation of
747 poro-elasto-plasticity soil model. *International Journal for Numerical and Analytical*
748 *Methods in Geomechanics*, 39(13): 1410-1430.
- 749 Tong, D., Liao, C. and Chen, J., 2019. Wave-monopile-seabed interaction considering nonlinear
750 pile-soil contact. *Computers and Geotechnics*, 113: 103076.
- 751 Tong, D., Liao, C., Jeng, D.-S., Zhang, L., Wang, J. and Chen, L., 2017. Three-dimensional modeling
752 of wave-structure-seabed interaction around twin-pile group. *Ocean Engineering*, 145:
753 416-429.
- 754 Tonkin, S., Yeh, H., Kato, F. and Sato, S., 2003. Tsunami scour around a cylinder. *Journal of Fluid*
755 *Mechanics*, 496: 165-192.
- 756 Tuković, Ž., Cardiff, P., Karac, A., Jasak, H. and Ivankovic, A., 2014. OpenFOAM Library for Fluid
757 Structure Interaction. *9th International OpenFOAM® Workshop*.
- 758 Twersky, V., 1952. Multiple scattering of radiation by an arbitrary configuration of parallel cylinders.
759 *The Journal of the Acoustical Society of America*, 24(1): 42-46.
- 760 Ulker, M. and Rahman, M., 2009. Response of saturated and nearly saturated porous media:
761 Different formulations and their applicability. *International journal for numerical and*
762 *analytical methods in geomechanics*, 33(5): 633-664.
- 763 Ulker, M.B.C., Rahman, M.S. and Jeng, D.-S., 2009. Wave-induced response of seabed: various
764 formulations and their applicability. *Applied Ocean Research*, 31(1): 12-24.
- 765 Wei, G., Kirby, J.T. and Sinha, A., 1999. Generation of waves in Boussinesq models using a source
766 function method. *Coastal Engineering*, 36(4): 271-299.
- 767 Ye, J., Jeng, D.-S., Chan, A., Wang, R. and Zhu, Q., 2016. 3D Integrated numerical model for
768 fluid–structures–seabed interaction (FSSI): Elastic dense seabed foundation. *Ocean*
769 *Engineering*, 115: 107-122.
- 770 Ye, J., Jeng, D.-S., Wang, R. and Zhu, C., 2013. A 3-D semi-coupled numerical model for
771 fluid–structures–seabed-interaction (FSSI-CAS 3D): Model and verification. *Journal of*
772 *Fluids and Structures*, 40: 148-162.
- 773 Zhang, J., Sun, K., Zhai, Y., Zhang, H. and Zhang, C., 2016. Physical Study on Interactions between

774 Waves and a Well-mixed Seabed. *Journal of Coastal Research*: 198-203.
775 Zhang, J.S., Jeng, D.-S. and Liu, P.L.F., 2011. Numerical study for waves propagating over a porous
776 seabed around a submerged permeable breakwater: PORO-WSSI II model. *Ocean*
777 *Engineering*, 38(7): 954-966.
778 Zhang, Q., Zhou, X.-L., Wang, J.-H. and Guo, J.-J., 2017. Wave-induced seabed response around an
779 offshore pile foundation platform. *Ocean Engineering*, 130: 567-582.
780 Zhao, H.Y. and Jeng, D.-S., 2016. Accumulated Pore Pressures around Submarine Pipeline Buried in
781 Trench Layer with Partial Backfills. *Journal of Engineering Mechanics, ASCE*: 04016042.
782 Zhao, H.Y., Jeng, D.S., Liao, C.C. and Zhu, J.F., 2017. Three-dimensional modeling of wave-induced
783 residual seabed response around a mono-pile foundation. *Coastal Engineering*, 128: 1-21.
784